



Investigation of Resonance Frequency and Stability of Solutions in a Continuous Rotor System

Amit Malgol¹ · K. P. Vineesh¹ · Ashesh Saha¹

Received: 9 November 2023 / Revised: 6 March 2024 / Accepted: 9 March 2024
© Springer Nature Singapore Pte Ltd. 2024

Abstract

Purpose The primary objective of this work is to analyze the effect of different system parameters on the resonance frequency of the linear rotor system. The effect of internal damping on the stability of the system is also investigated and a critical frequency ratio separating the stable and unstable regions is obtained.

Methods A continuous rotor system is modeled by considering some critical factors, like the gyroscopic and rotary inertia effects of disc and shaft cross-sections, internal damping, large shaft deformation, and restriction to shaft axial motion at the bearings. The bearings are replaced by spring-dashpot systems along both horizontal and vertical directions. The governing partial differential equations (PDE's) for the vibrations of the disc along the horizontal and vertical directions are derived by employing Hamilton's principle. The governing equations are then reduced to a set of ordinary differential equations (ODEs) using the method of modal projection. The large deformation, restriction to axial motion of the shaft, and the nonlinear stiffness of the end springs yield nonlinearities in the system governing equations. However, only the linear system is considered in this paper.

Results and Conclusion The parameters in the dimensionless form of the governing equations are functions of some independent variables. These independent variables, on the other hand, are associated with the material and geometrical properties of the rotor system. The effect of the independent parameters on the system dynamics is analysed wherein the variation of the dependent parameters is also monitored. An appropriate design of a rotor system can be achieved through a methodical analysis, like the one this study addresses.

Keywords Extended Hamilton's principle · Method of modal projection · Campbell diagram · Internal damping · Gyroscopic effect

List of Symbols

M_d	Mass of disk	I_{dy}	Polar mass moment of inertia of disk ($Y \Rightarrow$ axial direction of the disk)
L	Length of shaft	$I = AR_s^2$	Area moment of inertia of shaft cross-section
A	Cross sectional area of shaft	R_s	Radius of gyration of shaft cross-section
ρ	Density of shaft material	$L_1(l_1)$	Dimensional (dimensionless) disk position on shaft from left end bearing
e	Eccentricity of disk mass center away from the geometric center	$\Psi_1(y)$	1St orthonormal mode shape
I_{dx}	Mass moment of disc about horizontal (X -) direction (disk radial direction)	$t(\tau)$	Dimensional (dimensionless) time
		$U(Y, t)(u(y, \tau))$	Dimensional (dimensionless) displacement of disk along X - direction
		$W(Y, t)(w(y, \tau))$	Dimensional (dimensionless) displacement of disk along vertical (Z -) direction

✉ Amit Malgol
amitmalgol123@gmail.com

K. P. Vineesh
vineesh@nitc.ac.in

Ashesh Saha
ashesh@nitc.ac.in

¹ Department of Mechanical Engineering, National Institute of Technology Calicut, Kerala 673601, India

θ_x and θ_y	Rotational displacements about horizontal and vertical directions, respectively
T	Total kinetic energy of the rotor system
V	Total strain energy of the shaft
$r_e (= e/L)$	Dimensionless eccentricity ratio
$r_m (= \rho AL/M_d)$	Dimensionless mass ratio
$r = R_s/L$	Dimensionless radius of gyration
$r_g = I/AL^2 = r^2$	Shaft geometric parameter
$r_f (= \Omega/\Upsilon)$	Dimensionless frequency ratio
Ω	Spin speed of the rotor
$\Upsilon = \sqrt{EI/(\rho AL^4)}$	Natural frequency of shaft
$r_{dx} (= I_{dx}/\rho AL^3)$	Mass moment of inertia of the disc about x -axis
$r_{dy} (= I_{dy}/\rho AL^3)$	Mass moment of inertia of the disc about y -axis
ω_n	Undamped natural frequency (dimensionless) of the rotor system
G	Dimensionless gyroscopic coefficient
m_e	Effective mass
q_0	Amplitude of excitation (dimensionless)
δ	Dirac delta function
$C_{ex}(c_{ex})$	Dimensional (dimensionless) damping constant due to air resistance in horizontal direction
$C_{ez}(c_{ez})$	Dimensional (dimensionless) damping constant due to air resistance in vertical direction
$C_1(c_1)$	Dimensional (dimensionless) viscous damping constant of left bearing
$C_2(c_2)$	Dimensional (dimensionless) viscous damping constant of right bearing
$C_i(c_i)$	Dimensional (dimensionless) internal damping coefficient
μ_x and μ_z	Dimensionless damping factor in horizontal and vertical direction, respectively
μ_i	Internal Damping factor
$K_{11}(k_{11})$	Dimensional (dimensionless) linear spring coefficient along X - direction
$K_{21}(k_{21})$	Dimensional (dimensionless) linear spring coefficient along Z - direction
$K_{13}(k_{13})$	Dimensional (dimensionless) non-linear spring stiffness along X - direction
$K_{23}(k_{23})$	Dimensional (dimensionless) non-linear spring stiffness along Z - direction

Introduction

Rotating machinery such as turbines, compressors, and pumps are extensively used in various sectors like energy generation, power transmission, etc. Unavoidable eccentricity between the center of mass of the disc away from the center of rotation causes unwanted vibrations in high-speed rotating systems, resulting in unsafe working conditions as well as the depreciation of expensive equipment and infrastructure. These vibrations in rotating machinery may also lead to catastrophic fatigue failure. Many researchers attempt to identify an approach that can effectively control vibrations in the rotor system to avoid unwanted failure and minimize the energy loss. This can somewhat be achieved at the preliminary stages of design of a rotating system. An extensive analysis is performed in this paper to understand the effect of different parameters on the system response. The parameters in the rotor system modelled in this paper are functions of geometrical and material properties. Hence, the system vibrations can be related to these geometrical and material properties which, on the other hand, will help to achieve an effective design to minimize the amplitude of vibrations of the rotating system.

The literature consists of preliminary investigations on both linear and nonlinear rotor dynamics [1–5]. Several models are available in the literature for analysis of rotor system vibrations. They can be categorized into: (i) continuous model [6–28], and (ii) discrete or lumped parameter model [29–48]. In the lumped parameter model, inertia of the shaft is neglected in comparison to the inertia of the disc. The restoring force of the shaft is considered either a linear [45] or a nonlinear function [6, 7, 32, 34, 43, 47] of displacement of the disc. The bearing clearance is also assumed to provide a restoring force [5, 31, 39, 43, 47, 48]. Different models for the gyroscopic effect [29–32, 34, 35, 38, 40, 43, 45], hydrodynamic forces in the journal bearings [32, 43], internal damping [32, 33, 35, 43–48], etc., are available in the literature which can be conveniently used for the analysis of a discrete rotor system.

There is a considerable number of literatures on the analysis of continuous rotor systems [6–28] wherein the inertia of the shaft is also considered along with the inertia of the disc. In the continuous model, the governing equations of the shaft-rotor system are first derived in the form of partial differential equations (PDE's) either by using Lagrange's principle [3, 9, 12, 23] or Hamilton's principle [6, 11–15, 18, 21, 49–51]. Several important factors, like the large beam deflection [13–15], rotary inertia [11, 13, 14, 19, 22, 23], internal damping [6, 7, 23–26], etc., can be incorporated in the continuous system model. The transformation of the governing PDEs into a set of ODEs can be achieved by either Galerkin method [6, 18, 21], or Raleigh–Ritz method [3, 9, 11, 16, 23], or any other dimensionality reduction technique. In this

paper, a continuous rotor system is modelled by considering the effect of rotary inertia and gyroscopic moment of the disc and shaft cross sections, internal damping, large beam deflection and constraints to shaft's axial motion at bearings. The PDE's governing the system vibrations are obtained using Hamilton's principle for which the energy terms are derived by following the reference [3]. One of the novelties of this work is the reduction of PDEs to ODEs by Galerkin type method of modal projection using orthonormal mode shapes of a beam supported by Kelvin–Voigt model at both ends [22, 28].

The sources of nonlinearities in a rotor system model are: (i) the large deflection of the shaft [13–15], (ii) restriction to axial motion of the shaft at the bearings [3, 13–15], (iii) restoring force due to bearing clearance [5, 31, 32, 39, 43, 47], (iv) hydrodynamic forces in journal bearings [33, 44], etc. The effect of the geometric nonlinearities due to the large deflection of the shaft is negligible for small amplitude vibrations. In many practical cases, the effect of nonlinearities is negligibly small and the linear systems might provide reasonably accurate results. A lot of work on the analysis of linear systems are available in literatures [20, 22, 28, 45]. Analysis of the linear rotor system is essential to determine the effect of system parameters on the frequency response curves [22, 28], phase angle plot [22], critical speeds [20, 28, 45], forward and backward whirling motion [20, 28, 45], etc.

The geometric nonlinearities are triggered for large amplitude of oscillations in a rotor system. The analysis of a nonlinear rotor system may lead to some interesting results, such as fluttering [26], multivalued solutions [13–15, 25, 28, 37, 43, 47], subharmonic motion [30, 31, 35], quasiperiodic motion [16, 35], chaotic behaviour [16, 35], jump phenomena [13–15, 25, 28, 35, 43, 47], Hopf bifurcation [31, 43, 47], forward and backward whirling motion [18, 20, 28–31, 34, 38, 40, 41, 49–51], multiple loops [43, 47], Spring hardening [13–15, 28, 43, 48], etc. The study of linear and nonlinear rotor systems has distinct advantages, and both yields meaningful insights. Both analyses should be performed to have a better understanding of a rotor system. In this study, only the linear system is addressed, serving as a foundation for future analyses of the nonlinear system. The derivation of the continuous rotor system with the addition of various nonlinearities, as well as the effect of independent factors on the linear response, are discussed in this work.

The rest of the paper is organized as follows. In the section "Mathematical Modeling", the mathematical model of the rotor system is derived. The analytical method for obtaining the closed form solutions and the analysis of free vibration of the rotor system is covered in the section "Exact Analytical Solution and Analysis of Free Vibrations" followed by results and discussions in the section "Results and Discussion". At the end, some

conclusions about this present work are drawn and scopes for future work are presented.

Mathematical Modeling

The modelling of the rotor system and the derivation of the governing equations of motion are discussed in this section. The physical system is shown in Fig. 1 wherein a rigid disc is mounted on a flexible shaft supported by two bearings B_1 and B_2 . The flexibility of each of these two bearings is modelled by spring-dashpot systems along horizontal and vertical directions as shown in Fig. 1c and d. These springs at each bearing are assumed to be isotropic with cubic nonlinear stiffness. This cubic nonlinearity will result in the intended symmetric bending of the shaft in the $X - Y$ and $Z - Y$ planes [11]. The linear and nonlinear spring coefficients at bearing B_1 are K_{11} and K_{13} , respectively, and at bearing B_2 are K_{21} and K_{23} , respectively. Accordingly, the spring forces at bearings B_1 and B_2 along horizontal (X -) direction are $F_{sx1} = K_{11}U(0, t) + K_{13}U^3(0, t)$, and $F_{sx2} = K_{21}U(L, t) + K_{23}U^3(L, t)$, respectively, where $U(Y, t)$ is the displacement of the shaft along X - direction. The centrifugal force due to the eccentricity (e) of the center of mass (G) away from the geometric center (S) induces vibrations in the rotor system. The rotor system is modelled as a continuous system with the inclusion of several factors like (i) tilting motion of disc and shaft, (ii) gyroscopic effect of disc and shaft, (iii) internal damping, (iv) large deformation of shaft, and (v) restriction of shaft axial motion at the bearings. The partial differential equations governing the vibrations of the rotor system are derived by using the extended Hamilton's principle. The energy terms needed in the extended Hamilton's principle are obtained from [13–15]. The governing partial differential equations are reduced to a set of ordinary differential equations by the method of modal projection. In what follows, each of these steps are discussed in separate sections ("Derivation of Governing Equations Using Hamilton's Principle" and "Derivation of the Governing Ordinary Differential Equations by the Method of Modal Projection") for proper understanding of the development of the mathematical model.

Derivation of Governing Equations Using Hamilton's Principle

According to the Extended Hamilton's principle,

$$\int_{t_1}^{t_2} (\delta T - \delta V + \delta \bar{W}_{nc}) dt = 0, \quad (1)$$

where T and V are the total kinetic and potential energy of the rotor system, respectively, \bar{W}_{nc} is the work done by the nonconservative forces and δ represents the variation. The kinetic energy of the disc and the shaft are given by [13–15].

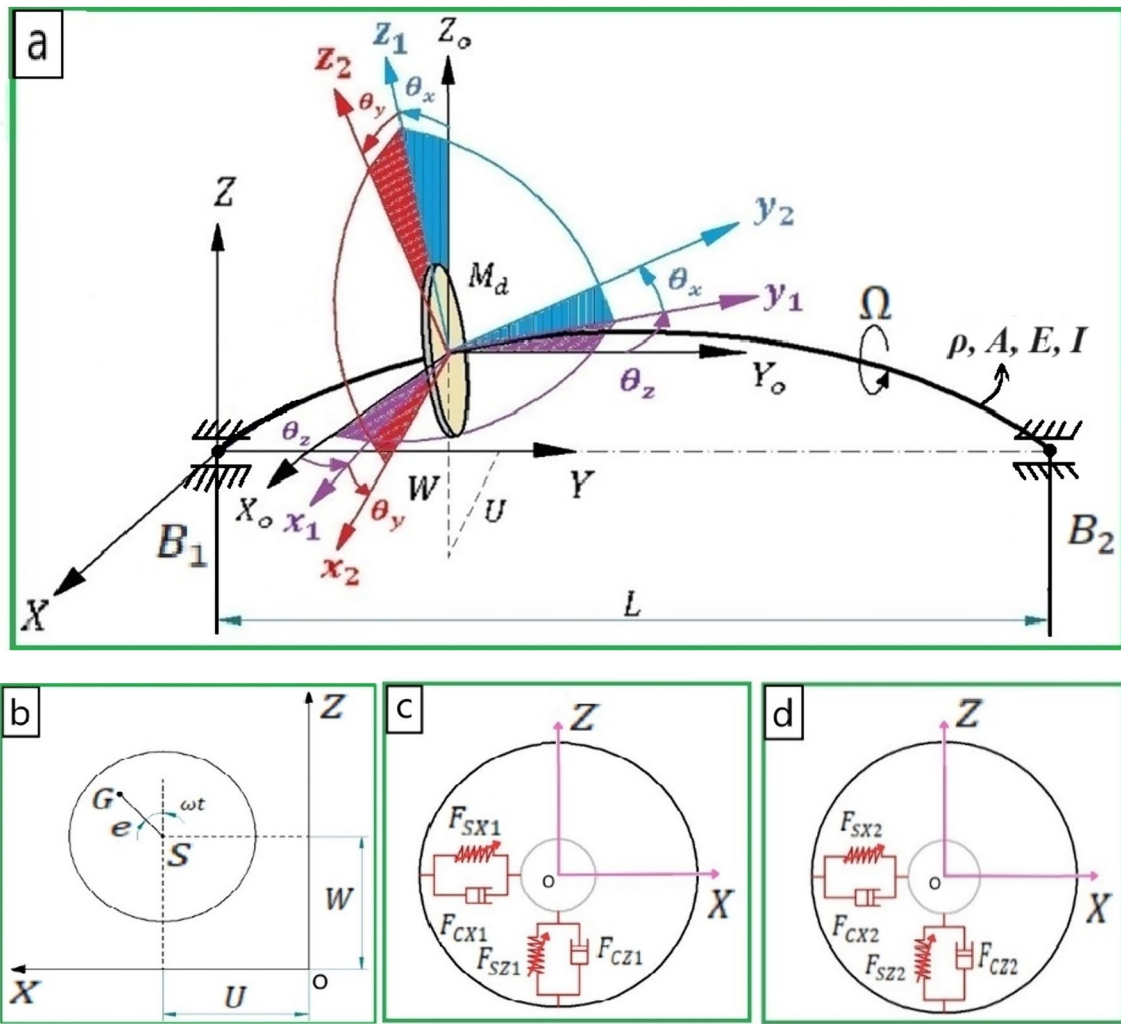


Fig. 1 Schematic representation of a disk rotating on a flexible shaft, b rotor eccentricity, c bearing B₁ (Left), and d bearing B₂ (Right)

$$\begin{aligned}
 T_d &= T_{d1} + T_{d2} + T_{d3} + T_{d4} \\
 &= \left[\frac{M_d}{2} (\dot{U}^2 + \dot{W}^2) + \frac{I_{dx}}{2} (\dot{\theta}_x^2 + \dot{\theta}_z^2) \right. \\
 &\quad \left. + I_{dy} \Omega \dot{\theta}_z \theta_x + M_d \Omega e (\dot{U} \cos \Omega t - \dot{W} \sin \Omega t) \right]_{L_1}, \tag{2a}
 \end{aligned}$$

$$\begin{aligned}
 T_s &= T_{s1} + T_{s2} + T_{s3} \\
 &= \int_0^L \frac{\rho I}{2} (\theta_x^2 + \theta_z^2) dY + \int_0^L \frac{\rho A}{2} (\dot{U}^2 + \dot{W}^2) dY \\
 &\quad + \int_0^L 2\rho I \Omega \dot{\theta}_z \theta_x dY, \tag{2b}
 \end{aligned}$$

respectively, where $\dot{U} = \frac{\partial U}{\partial t}$, $\dot{W} = \frac{\partial W}{\partial t}$, $\theta_x = \frac{\partial W}{\partial Y}$, $\theta_z = -\frac{\partial U}{\partial Y}$, $\dot{\theta}_x = \frac{\partial \theta_x}{\partial t} = \frac{\partial^2 W}{\partial t \partial Y}$, and $\dot{\theta}_z = \frac{\partial \theta_z}{\partial t} = -\frac{\partial^2 U}{\partial t \partial Y}$. The subscript L_1 in

Eq. (2a) indicates that the quantities \dot{U} , \dot{W} , θ_x , θ_z , $\dot{\theta}_x$, and $\dot{\theta}_z$ are evaluated at $Y = L_1$, which is the location of the disk on the shaft. The total kinetic energy of the rotor system is $T = T_d + T_s$. T_{d1} refers to kinetic energy due to the translational motion of the disk, T_{d2} refers to kinetic energy due to the rotational motion of the disk, T_{d3} refers to the gyroscopic effect of the disk, T_{d4} refers to the centrifugal force acting on the disk, T_{s1} refers to kinetic energy of the shaft in bending, T_{s2} refers to the rotary inertia of the shaft, and T_{s3} refers to the gyroscopic effect of the shaft.

The strain energy of the shaft (V_{sh}) and spring (V_{sp}) are given by [13–15]

$$\begin{aligned}
 V_{sh} = & \int_0^L \frac{EI}{2} \left\{ \left(\frac{\partial \theta_x}{\partial Y} \right)^2 + \left(\frac{\partial \theta_z}{\partial Y} \right)^2 \right\} dY \\
 & + \int_0^L \frac{EA}{2} \left(\frac{1}{4} \theta_x^4 + \frac{1}{4} \theta_z^4 + \frac{1}{2} \theta_x^2 \theta_z^2 \right) dY \quad (3a) \\
 & + \int_0^L \frac{EA}{4L} \left(\int_0^L (\theta_x^2 + \theta_z^2) dY \right) (\theta_x^2 + \theta_z^2) dY,
 \end{aligned}$$

$$\begin{aligned}
 V_{sp} = & \int_0^L \left\{ \frac{1}{2} K_{11} (U^2 + W^2) + \frac{1}{4} K_{13} (U^4 + W^4) \right\} \delta(Y) dY \\
 & + \int_0^L \left\{ \frac{1}{2} K_{21} (U^2 + W^2) + \frac{1}{4} K_{23} (U^4 + W^4) \right\} \delta(Y - L) dY, \quad (3b)
 \end{aligned}$$

respectively, where δ is the Dirac delta function. The first and second integrals in Eq. (3a) are the strain energy of the shaft with the second integral being associated with the higher order deformation of the shaft. The third integral is the strain energy due to the constraint to axial motion of the shaft at the bearings. As mentioned earlier, both the bearings at $Y = 0$ and $Y = L$ are considered to be flexible and are replaced by springs with nonlinear stiffness. Moreover, the stiffness of the two bearings are

assumed to be different. The potential energy due to the deformation of the springs at the supports are given by Eq. (3b).

The variation in work done by the nonconservative forces are given by [16, 21, 27, 28]

$$\begin{aligned}
 \delta \bar{W}_{nc} = & \int_0^L \left(C_{ex} \frac{\partial U}{\partial t} \delta U + C_{ez} \frac{\partial W}{\partial t} \delta W \right) dY \\
 & + \int_0^L C_1 \left(\frac{\partial U}{\partial t} \delta U + \frac{\partial W}{\partial t} \delta W \right) \delta(Y) dY \quad (4) \\
 & + \int_0^L C_2 \left(\frac{\partial U}{\partial t} \delta U + \frac{\partial W}{\partial t} \delta W \right) \delta(Y - L) dY,
 \end{aligned}$$

where C_{ex} and C_{ez} are the external damping coefficients along horizontal and vertical directions, respectively. These external damping are caused by the resistance of the surrounding fluid (air or steam) on the rotor system. They are assumed to be viscous in nature for the simplicity of analysis. The bearings are considered to be isotropic with damping coefficients C_1 and C_2 for the left (at $Y = 0$) and right (at $Y = L$) bearings, respectively.

Substitution of Eqs. (2)–(4) into Eq. (1) leads to the partial differential equations governing the vibrations of the rotor system along horizontal and vertical directions as

$$\begin{aligned}
 \rho A \frac{\partial^2 U}{\partial t^2} + EI \frac{\partial^4 U}{\partial Y^4} + M_d \frac{\partial^2 U}{\partial t^2} \delta_{L_1} - I_{dx} \frac{\partial}{\partial Y} \left(\frac{\partial^3 U}{\partial t^2 \partial Y} \delta_{L_1} \right) + I_{dy} \Omega \frac{\partial}{\partial Y} \left(\frac{\partial^2 W}{\partial t \partial Y} \delta_{L_1} \right) \\
 - \rho I \frac{\partial^4 U}{\partial t^2 \partial Y^2} + 2\rho I \Omega \frac{\partial^3 W}{\partial t \partial Y^2} - \frac{EA}{2} \frac{\partial}{\partial Y} \left\{ \frac{\partial U}{\partial Y} \left(\left(\frac{\partial U}{\partial Y} \right)^2 + \left(\frac{\partial W}{\partial Y} \right)^2 \right) \right\} \quad (5a)
 \end{aligned}$$

$$\begin{aligned}
 - \frac{EA}{L} \frac{\partial^2 U}{\partial Y^2} \int_0^L \left(\left(\frac{\partial U}{\partial Y} \right)^2 + \left(\frac{\partial W}{\partial Y} \right)^2 \right) dY + (K_{11} U + K_{13} U^3) \delta(Y) + (K_{21} U + K_{23} U^3) \delta_L \\
 + C_{ex} \frac{\partial U}{\partial t} + C_1 \frac{\partial U}{\partial t} \delta(Y) + C_2 \frac{\partial U}{\partial t} \delta_L + C_i I \frac{\partial^5 U}{\partial Y^4 \partial t} + \Omega C_i I \frac{\partial^4 W}{\partial Y^4} = M_d \Omega^2 e \sin \Omega t \delta_{L_1}, \text{ and}
 \end{aligned}$$

(5b)

$$\begin{aligned}
 \rho A \frac{\partial^2 W}{\partial t^2} + EI \frac{\partial^4 W}{\partial Y^4} + M_d \frac{\partial^2 W}{\partial t^2} \delta_{L_1} - I_{dx} \frac{\partial}{\partial Y} \left(\frac{\partial^3 W}{\partial Y \partial t^2} \delta_{L_1} \right) - I_{dy} \Omega \frac{\partial}{\partial Y} \left(\frac{\partial^2 U}{\partial t \partial Y} \delta_{L_1} \right) \\
 - \rho I \frac{\partial^4 W}{\partial t^2 \partial Y^2} - 2\rho I \Omega \frac{\partial^3 U}{\partial t \partial Y^2} - \frac{EA}{2} \frac{\partial}{\partial Y} \left\{ \frac{\partial W}{\partial Y} \left(\left(\frac{\partial U}{\partial Y} \right)^2 + \left(\frac{\partial W}{\partial Y} \right)^2 \right) \right\} \\
 - \frac{EA}{L} \frac{\partial^2 W}{\partial Y^2} \int_0^L \left(\left(\frac{\partial U}{\partial Y} \right)^2 + \left(\frac{\partial W}{\partial Y} \right)^2 \right) dY + (K_{11} W + K_{13} W^3) \delta(Y) + (K_{21} W + K_{23} W^3) \delta_L \\
 + C_{ez} \frac{\partial W}{\partial t} + C_1 \frac{\partial W}{\partial t} \delta(Y) + C_2 \frac{\partial W}{\partial t} \delta_L + C_i I \frac{\partial^5 W}{\partial Y^4 \partial t} - \Omega C_i I \frac{\partial^4 U}{\partial Y^4} = M_d \Omega^2 e \cos \Omega t \delta_{L_1},
 \end{aligned}$$

respectively, where $\delta_{L_1} = \delta(Y - L_1)$, and $\delta_L = \delta(Y - L)$. Note the difference between the symbols δ (in Eq. (1)) and δ ; the first one is used to represent the variation and the second one for the Dirac delta function. Also note that the last two terms associated with C_i in Eqs. (5a) and (5b) are the bending moments due to the strain rate dependent internal damping along X and Z axes, respectively [23–26]. Introducing the dimensionless parameters.

$$u = \frac{U}{L}, \quad y = \frac{Y}{L}, \quad w = \frac{W}{L}, \quad \tau = \Upsilon t, \quad \Upsilon = \sqrt{\frac{EI}{\rho AL^4}}, \quad l_1 = \frac{L_1}{L}$$

$$r_m = \frac{\rho AL}{M_d}, \quad r_{dx} = \frac{I_{dx}}{\rho AL^3}, \quad r_{dy} = \frac{I_{dy}}{\rho AL^3}, \quad r_e = \frac{e}{L}, \quad r_f = \frac{\Omega}{\Upsilon}$$

$$r_g = \frac{I}{AL^2} = \frac{AR_s^2}{AL^2} = r^2, k_{11} = \frac{K_{11}L^3}{EI}, \quad k_{21} = \frac{K_{21}L^3}{EI}, \quad k_{13} = \frac{K_{13}L^2}{M_d\Upsilon^2}$$

$$k_{23} = \frac{K_{23}L^2}{M_d\Upsilon^2}, \quad c_{ex} = \frac{C_{ex}L}{M_d\Upsilon}, \quad c_{ez} = \frac{C_{ez}L}{M_d\Upsilon}, \quad c_1 = \frac{C_1}{M_d\Upsilon}, \quad c_2 = \frac{C_2}{M_d\Upsilon}$$

$$c_i = \frac{C_i I}{M_d \Upsilon L^3},$$

the governing Eq. (5) are reduced to the dimensionless forms as

$$(r_m + \delta_{l_1}) \frac{\partial^2 u}{\partial \tau^2} + r_m \frac{\partial^4 u}{\partial y^4} - r_m r_{dx} \frac{\partial}{\partial y} \left(\frac{\partial^3 u}{\partial \tau^2 \partial y} \delta_{l_1} \right) + r_m r_{dy} r_f \frac{\partial}{\partial y} \left(\frac{\partial^2 w}{\partial \tau \partial y} \delta_{l_1} \right) - r_g r_m \frac{\partial^4 u}{\partial \tau^2 \partial y^2}$$

$$+ 2r_m r_g r_f \frac{\partial^3 w}{\partial \tau \partial y^2} - \frac{r_m}{2r_g} \frac{\partial}{\partial y} \left(\frac{\partial u}{\partial y} \left(\left(\frac{\partial u}{\partial y} \right)^2 + \left(\frac{\partial w}{\partial y} \right)^2 \right) \right) - \frac{r_m}{r_g} \frac{\partial^2 u}{\partial y^2} \int_0^L \left(\left(\frac{\partial u}{\partial y} \right)^2 + \left(\frac{\partial w}{\partial y} \right)^2 \right) dy +$$

$$(k_{11} r_m u + k_{13} u^3) \delta(y) + (k_{21} r_m u + k_{23} u^3) \delta_l + c_{ex} \frac{\partial u}{\partial \tau} + c_1 \frac{\partial u}{\partial \tau} \delta(y) + c_2 \frac{\partial u}{\partial \tau} \delta_l$$

$$+ c_i \frac{\partial^5 u}{\partial y \partial \tau} + r_f c_i \frac{\partial^4 w}{\partial y^4} = r_e r_f^2 \sin(r_f \tau) \delta_{l_1}, \text{ and}$$

$$(r_m + \delta_{l_1}) \frac{\partial^2 w}{\partial \tau^2} + r_m \frac{\partial^4 w}{\partial y^4} - r_m r_{dx} \frac{\partial}{\partial y} \left(\frac{\partial^3 w}{\partial \tau^2 \partial y} \delta_{l_1} \right) - r_m r_{dy} r_f \frac{\partial}{\partial y} \left(\frac{\partial^2 u}{\partial \tau \partial y} \delta_{l_1} \right) - r_m r_g \frac{\partial^4 w}{\partial \tau^2 \partial y^2}$$

$$- 2r_m r_g r_f \frac{\partial^3 u}{\partial \tau \partial y^2} - \frac{r_m}{2r_g} \frac{\partial}{\partial y} \left(\frac{\partial w}{\partial y} \left(\left(\frac{\partial u}{\partial y} \right)^2 + \left(\frac{\partial w}{\partial y} \right)^2 \right) \right) - \frac{r_m}{r_g} \frac{\partial^2 w}{\partial y^2} \int_0^L \left(\left(\frac{\partial u}{\partial y} \right)^2 + \left(\frac{\partial w}{\partial y} \right)^2 \right) dy$$

$$+ (k_{11} r_m w + k_{13} w^3) \delta(y) + (k_{21} r_m w + k_{23} w^3) \delta_l + c_{ez} \frac{\partial w}{\partial \tau} + c_1 \frac{\partial w}{\partial \tau} \delta(y) + c_2 \frac{\partial w}{\partial \tau} \delta_l$$

$$+ c_i \frac{\partial^5 w}{\partial y \partial \tau} - r_f c_i \frac{\partial^4 u}{\partial y^4} = r_e r_f^2 \cos(r_f \tau) \delta_{l_1},$$

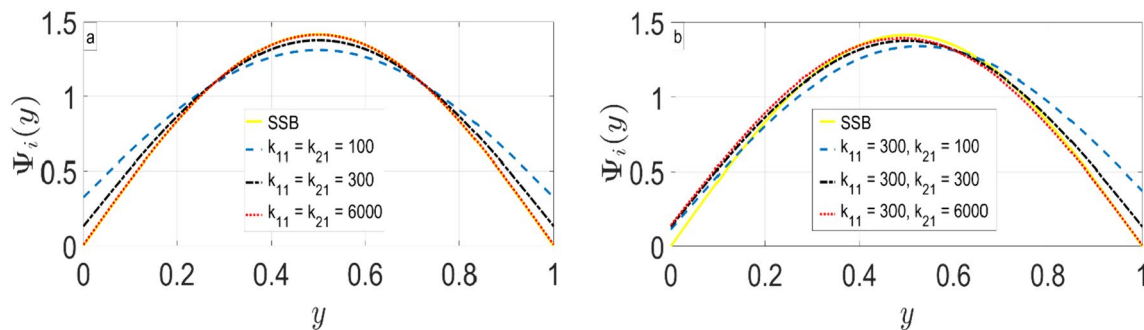


Fig. 2 Comparison of mode shapes of a beam with springs attached at both ends with that for a simply supported beam (SSB)

$$u(y, \tau) = \sum_{i=1}^n \Psi_i(y)u_i(\tau), \text{ and } w(y, \tau) = \sum_{i=1}^n \Psi_i(y)w_i(\tau), \quad (7)$$

where $\Psi_i(y)$ is the i th orthonormal mode shape of a reduced system consisting of a beam supported by springs at the ends. For motion along x -direction, the beam is subjected to the boundary conditions: $\frac{\partial^2 u}{\partial y^2} \Big|_{y=0} = 0, \frac{\partial^3 u}{\partial y^3} \Big|_{y=0} = -k_{11}u, \frac{\partial^2 u}{\partial y^2} \Big|_{y=1} = 0, \text{ and } \frac{\partial^3 u}{\partial y^3} \Big|_{y=1} = k_{21}u$. The boundary conditions for motion along z -direction is obtained by replacing u by w in these expressions. The i th orthonormal mode shape $\Psi_i(y)$ is obtained as [22]

$$\Psi_i(y) = C_1 \left[(\sin p_i y + \sinh p_i y) + C_2 \left(\cos p_i y + \cosh p_i y - \frac{2k_{11}}{p_i^3} \sinh p_i y \right) \right]. \quad (8)$$

where $C_2 = p_i^3 (\sinh p_i - \sin p_i) / (2k_{11} \sinh p_i + p_i^3 (\cos p_i - \cosh p_i))$. The eigenvalue p_i can be determined from the following characteristic equation

$$p_i^6 (1 - \cos p_i \cosh p_i) + p_i^3 (k_{11} + k_{21}) (\cos p_i \sinh p_i - \sin p_i \cosh p_i) + 2k_{11}k_{21} \sin p_i \sinh p_i = 0. \quad (9)$$

Imposing the conditions $k_{11} \rightarrow \infty, \text{ and } k_{21} \rightarrow \infty$ for hard bearings in Eq. (9) leads to

$$\sin p_i = 0. \quad (10)$$

This is the characteristic equation for a simply supported beam (SSB). The i th eigenvalue obtained from Eq. (10) is $p_i = i\pi$. The mode shape $\Psi_i(y)$ satisfy the following orthonormality conditions

$$\int_0^1 \Psi_i(y)\Psi_j(y)dy = \delta_{ij}, \text{ and } \int_0^1 \Psi_i \frac{d^4 \Psi_j}{dy^4} dy = \int_0^1 \Psi_j \frac{d^4 \Psi_i}{dy^4} dy = p_i^4 \delta_{ij}. \quad (11)$$

The arbitrary constant C_1 in Eq. (8) is rendered unique through the normalization scheme $\int_0^1 \Psi_i^2(y)dy = 1$. The expression for this constant C_1 obtained using the software package ‘‘MAPLE’’ is long and not shown in this paper.

The orthonormal mode shape for the first mode ($\Psi_1(y)$) is plotted in Fig. 2 for different values of spring constants and compared with that for a simply supported beam (SSB). The bearings are assumed to be identical ($k_{11} = k_{21}$) in Fig. 2a. As a result, the mode shape is symmetric about $y = 0.5$. In Fig. 2b, the stiffness of the bearings differs causing the symmetry of the mode shape about $y = 0.5$ to break down. As shown in Fig. 2, the curve for $\Psi_1(y)$ for the beam with springs at both ends gradually approaches the mode shape curve for the simply supported beam and the difference is hardly noticeable for $k_{11} = k_{21} = 6000$. It is to be noted that

the natural frequency for the first mode of vibrations for a SSB obtained from Eq. (10) is $p_1 = \pi$. Also, the orthonormal mode shapes for a SSB can be obtained as $\Psi_i(y) = \sqrt{2} \sin p_i y$.

To derive the governing ODEs, solutions (7) are first substituted into Eq. (6). The resulting equations are multiplied by the j th mode shape $\Psi_j(y)$ and integrated over the domain $[0, 1]$. The governing ODEs are then obtained by applying the orthonormality conditions (11). For the first mode of analysis ($i = j = 1$), the ODEs are obtained as

$$u_1'' + \mu_x u_1' + Gr_f w_1' + \omega_n^2 u_1 + \mu_i r_f w_1 + ((\lambda + \nu)u_1^3 + \lambda u_1 w_1^2) = q_0 \sin(r_f \tau), \quad (12a)$$

$$w_1'' + \mu_z w_1' - Gr_f u_1' + \omega_n^2 w_1 - \mu_i r_f u_1 + (\lambda w_1 u_1^2 + (\lambda + \nu)w_1^3) = q_0 \cos(r_f \tau), \quad (12b)$$

where the primes ($'$) denote derivative with respect to the dimensionless time τ and

$$\mu_{x,z} = (c_{eq})_{x,z} / m_e, (c_{eq})_{x,z} = c_{ex,ez} + c_i p_1^4 + c_1 (\Psi_1(0))^2 + c_2 (\Psi_1(1))^2, \quad (13a)$$

$$\mu_i = c_i p_1^4 / m_e, \omega_n^2 = \frac{r_m}{m_e} (p_1^4 + k_{11} (\Psi_1(0))^2 + k_{21} (\Psi_1(1))^2), \quad (13b)$$

$$q_0 = \frac{\Psi_1(t_1)}{m_e} r_e r_f^2,$$

$$m_e = (r_m + t_4 - D_r r_{dx} r_m (t_5 - t_6) - S_r r_g r_m t_1), \lambda = -\frac{r_m}{m_e r_g} \left(\frac{3}{2} t_3 L_b + S_{ra} t_1 t_2 \right), \quad (13c)$$

$$G = \frac{r_m}{m_e} (D_g r_{dy} (t_5 - t_6) + 2S_g r_g t_1), \nu = k_{13} (\Psi_1(0))^4 + k_{23} (\Psi_1(1))^4, \quad (13d)$$

$$t_1 = \int_0^1 \Psi_1 \frac{d^2 \Psi_1}{dy^2} dy, t_2 = \int_0^1 \left(\frac{d\Psi_1}{dy} \right)^2 dy, t_3 = \int_0^1 \Psi_1 \left(\frac{d\Psi_1}{dy} \right)^2 \left(\frac{d^2 \Psi_1}{dy^2} \right) dy, t_4 = \Psi_1^2(t_1), t_5 = \Psi_1(t_1) \frac{d^2 \Psi_1}{dy^2} \Big|_{y=l_1}, t_6 = \frac{d}{dy} \left(\Psi_1 \frac{d\Psi_1}{dy} \right) \Big|_{y=l_1}.$$

In Eq. (13c), the terms D_r and S_r are associated with the rotary inertia of the disc and shaft, respectively. Similarly, the terms D_g and S_g in Eq. (13d) are associated with the gyroscopic effects of the disc and shaft cross-sections, respectively. Moreover L_b is associated with the large beam deflection criterion, and S_{ra} is associated with the effect of restricting the shaft axial motion at the bearings. These terms may take a value of either 1 or 0 depending on whether the related effect is considered in the analysis or not, e.g., $D_r = 1$ if the disc rotary is considered in the analysis, and $L_b = 0$ if the large beam deflection criterion is not considered in the analysis. The expressions for t_1 to t_6 in Eq. (13e) are obtained using the software package “MAPLE”. They are long and are not presented in this paper.

The nonlinearities in the rotor system governed by Eq. (12) are associated with the parameters λ and ν . The large beam deflection and the shaft's confinement to axial motion are two elements that contribute to the nonlinearities related to λ . The parameter ν is a function of the cubic stiffness of the bearings (k_{13} and k_{23}). A rotor system associated with such nonlinear terms show some interesting results, like multiple solutions, jump phenomena, multiple loops, etc. [11, 13–15, 28, 43, 47]. The system parameters like λ, ν, G , etc., are treated as independent in many literatures [31, 38]. However, it is clear from Eqs. (12) and (13) that these parameters depend on the material and geometric properties of the rotor system. Arbitrarily choosing these parameters (λ, ν, G , etc.) may yield some undesired system dynamics.

In many practical applications, the deflection of the shaft may not be large enough and the shaft may move freely inside the bearings along axial direction. On top of that, if hard bearings are used, the nonlinearities may not be triggered. The system dynamics can then be predicted from the analysis of the linear system only (considering $\lambda = 0$ and $\nu = 0$). The analysis of the linear system is much easier compared to that for the nonlinear system as an exact analytical solution can easily be obtained. Moreover, the primary resonance condition of a linear system can easily be predicted. Considering all these important factors, a separate study is conducted in this paper on the analysis of a linear system for the continuous rotor model developed in this section. We primarily focus on the influence of different system parameters on the natural frequency of the continuous rotor system. The stability of the rotor system is additionally discussed in relation to the impact of internal damping. The exact analytical solution of the linear system is derived in the next section.

Exact Analytical Solution and Analysis of Free Vibrations

The exact closed form solutions of the linear system are first obtained in this section. The governing equations of the linear system obtained by substituting $\lambda = 0$ and $\nu = 0$ in Eq. (12) is written in the matrix form as

$$\tilde{\mathbf{I}}\tilde{\mathbf{x}}'' + \mathbf{D}\tilde{\mathbf{x}}' + \mathbf{F}\tilde{\mathbf{x}} = \tilde{\mathbf{Q}}_1\text{Im}(e^{ir_f\tau}) + \tilde{\mathbf{Q}}_2\text{Re}(e^{ir_f\tau}), \tag{14}$$

where \mathbf{I} is a 2×2 identity matrix and

$$\tilde{\mathbf{x}} = \begin{Bmatrix} u_1 \\ w_1 \end{Bmatrix}, \mathbf{D} = \begin{bmatrix} \mu_x & Gr_f \\ -Gr_f & \mu_z \end{bmatrix},$$

$$\mathbf{F} = \begin{bmatrix} \omega_n^2 & \mu_i r_f \\ -\mu_i r_f & \omega_n^2 \end{bmatrix}, \tag{15}$$

$$\tilde{\mathbf{Q}}_1 = \begin{Bmatrix} q_0 \\ 0 \end{Bmatrix}, \tilde{\mathbf{Q}}_2 = \begin{Bmatrix} 0 \\ q_0 \end{Bmatrix},$$

where $q_0 = \gamma r_e r_f^2$, and $\text{Im}(e^{ir_f\tau}) (= \sin(r_f\tau))$ and $\text{Re}(e^{ir_f\tau}) (= \cos(r_f\tau))$ are the imaginary and real parts of $e^{ir_f\tau}$, respectively. The solution of the linear system is first obtained for the excitations $\tilde{\mathbf{Q}}_1\text{Im}(e^{ir_f\tau})$ and $\tilde{\mathbf{Q}}_2\text{Re}(e^{ir_f\tau})$. Applying the principle of superposition, the solutions of Eq. (14) are finally obtained as [2]

$$u_1(\tau) = u_{11}(\tau) + u_{12}(\tau) = U_1 \sin(r_f\tau - \phi_x), \tag{16a}$$

$$w_1(\tau) = w_{11}(\tau) + w_{12}(\tau) = W_1 \cos(r_f\tau - \phi_z), \tag{16b}$$

where

$$U_1 \sin\phi_x = \frac{q_0}{\Delta} \left[\Delta_r \left((z_{12})_r - (z_{22})_i \right) + \Delta_i \left((z_{22})_r + (z_{12})_i \right) \right], \tag{17a}$$

$$U_1 \cos\phi_x = \frac{q_0}{\Delta} \left[\Delta_r \left((z_{22})_r + (z_{12})_i \right) + \Delta_i \left((z_{22})_i - (z_{12})_r \right) \right], \tag{17b}$$

$$W_1 \sin\phi_z = \frac{q_0}{\Delta} \left[\Delta_r \left((z_{12})_r - (z_{11})_i \right) + \Delta_i \left((z_{11})_r + (z_{12})_i \right) \right], \tag{17c}$$

$$W_1 \cos\phi_z = \frac{q_0}{\Delta} \left[\Delta_r \left((z_{11})_r + (z_{12})_i \right) + \Delta_i \left((z_{11})_i - (z_{12})_r \right) \right], \tag{17d}$$

$$\Delta = \Delta_r^2 + \Delta_i^2,$$

$$\Delta_r = (z_{11})_r (z_{22})_r - (z_{11})_i (z_{22})_i + (z_{12})_r^2 - (z_{12})_i^2, \tag{17e}$$

$$\Delta_i = (z_{11})_r (z_{22})_i + (z_{11})_i (z_{22})_r + 2(z_{12})_r (z_{12})_i,$$

$$(z_{11})_r = (z_{22})_r = \omega_n^2 - r_f^2, (z_{11})_i = r_f \mu_x, \tag{17f}$$

$$(z_{22})_i = r_f \mu_z, (z_{12})_r = \mu_i r_f, (z_{12})_i = r_f^2 G,$$

$$U_1 = \sqrt{(U_1 \sin \phi_x)^2 + (U_1 \cos \phi_x)^2}, \phi_x = \tan^{-1} \left(\frac{U_1 \sin \phi_x}{U_1 \cos \phi_x} \right), \tag{17g}$$

$$W_1 = \sqrt{(W_1 \sin \phi_z)^2 + (W_1 \cos \phi_z)^2}, \phi_z = \tan^{-1} \left(\frac{W_1 \sin \phi_z}{W_1 \cos \phi_z} \right). \tag{17h}$$

To plot the Campbell diagram, it is necessary to first derive the expression for the damped natural frequency. Equations governing the free vibrations are obtained in matrix form from Eq. (14) as

$$\mathbf{\tilde{I}\ddot{x}}'' + \mathbf{\tilde{D}\dot{x}}' + \mathbf{\tilde{F}x} = 0. \tag{18}$$

The solution of Eq. (18) can be assumed in the form as $\tilde{x} = (u_1 \ w_1)^T = (u_{10} \ w_{10})^T e^{\beta\tau} = \tilde{x}_0 e^{\beta\tau}$. Substitution of this assumed solution in Eq. (18) leads to

$$\mathbf{B}\tilde{x}_0 = 0, \tag{19}$$

where $\mathbf{B} = \begin{bmatrix} \beta^2 + \mu_x \beta + \omega_n^2 & Gr_f \beta + \mu_i r_f \\ -Gr_f \beta - \mu_i r_f & \beta^2 + \mu_z \beta + \omega_n^2 \end{bmatrix}$. For nontrivial solutions of \tilde{x}_0 (u_{10} , and w_{10}), the determinant of matrix \mathbf{B} should be zero ($|\mathbf{B}| = 0$). This leads to a quartic equation of β as

$$\beta^4 + (\mu_x + \mu_z)\beta^3 + (\mu_x \mu_z + 2\omega_n^2 + G^2 r_f^2)\beta^2 + ((\mu_x + \mu_z)\omega_n^2 + 2Gr_f^2 \mu_i)\beta + \omega_n^4 + \mu_i^2 r_f^2 = 0. \tag{20}$$

The roots of Eq. (20) are obtained numerically. Two sets of complex conjugate roots are obtained for the set of parameters chosen for the analysis. The imaginary parts of the roots correspond to the damped natural frequency. These are used to plot the Campbell diagrams to be discussed in the next section.

A closed form solution for the damped natural frequency can be determined for a special case of equal damping along horizontal and vertical directions ($\mu_x = \mu_z = \mu$). For $\mu_x = \mu_z = \mu$, Eq. (18) can be represented in terms of a complex variable $\eta(\tau) = w_1(\tau) + iu_1(\tau)$ as

$$\eta'' + \mu\eta' + \omega_n^2\eta + iGr_f\eta' + i\mu_i = 0. \tag{21}$$

Substituting the solution of the form of $\eta = \eta_0 e^{\beta\tau}$ in Eq. (21) yields

$$\beta^2 + (\mu + iGr_f)\beta + \omega_n^2 + i\mu_i = 0. \tag{22}$$

To separate the real and imaginary parts, β is written in terms of complex number form as

$$\beta = \beta_r + i\beta_i. \tag{23}$$

Substituting Eq. (23) into Eq. (21) and separating the real and imaginary parts leads to two equations which are solved to get

$$\beta_r = -\frac{\mu}{2} \pm \frac{\sqrt{(\mu^2 - 4\omega_n^2 - G^2 r_f^2) + \sqrt{(\mu^2 - 4\omega_n^2 - G^2 r_f^2)^2 + 4r_f^2(\mu G - 2\mu_i)^2}}}{2\sqrt{2}}, \tag{24a}$$

$$\beta_i = -\frac{Gr_f}{2} \mp \frac{\sqrt{-(\mu^2 - 4\omega_n^2 - G^2 r_f^2) + \sqrt{(\mu^2 - 4\omega_n^2 - G^2 r_f^2)^2 + 4r_f^2(\mu G - 2\mu_i)^2}}}{2\sqrt{2}}. \tag{24b}$$

Table 1 Independent parameters and its values

Independent parameter	c_{ex} , and c_{ez}	c_1 , and c_2	c_i	r_e	r_m
Value	0.00085	0.08	0	0.0001	0.1
Independent parameter	r_{dx}	r_{dy}	r	k_{11}	k_{21}
Value	0.05	0.1	0.1	500	500

These expressions are obtained by imposing the condition that β_r and β_i are real numbers. It is to be noted that β_i is the damped natural frequency of the linear system (18). Moreover, the solution of (18) is stable for a negative value of β_r . Positive value of β_r will lead to an exponentially growing solution. Imposing the condition for stable solution ($\beta_r \leq 0$) leads to

$$r_f \leq (r_f)_c, (r_f)_c = \frac{\left(\frac{\mu_i + \mu_o}{\mu_i}\right)\omega_n}{\sqrt{1 - \left(\frac{\mu_i + \mu_o}{\mu_i}\right)G}}, \tag{25}$$

where $\mu_o = (c_e + c_1(\Psi_1(0))^2 + c_2(\Psi_1(1))^2)/m_e$, $c_e = c_{ex} = c_{ez}$. Hence, the solution of Eq. (19) is unstable (exponentially growing) for frequency ratios above the critical value $(r_f)_c$. Solution of Eq. (21) is the homogeneous solution of Eq. (14) for $\mu_x = \mu_z = \mu$. As a consequence, the response of the rotor system governed by Eq. (14) (for $\mu_x = \mu_z = \mu$) will be unstable for $r_f > (r_f)_c$. Since $(r_f)_c = \infty$ for $\mu_i = 0$, the rotor system will always be stable in the absence of internal damping.

If the gyroscopic effect is neglected ($G = 0$), the critical frequency ratio is reduced to

$$(r_f)_c = \left(\frac{\mu_i + \mu_o}{\mu_i}\right)\omega_n. \tag{26}$$

Further, if all the external damping effects are neglected ($\mu_o = 0$),

$$(r_f)_c = \omega_n. \tag{27}$$

All the relevant and important results are discussed in the next section. In most of the cases, the rotor system

dynamics are analyzed through the frequency response and phase angle plots.

Results and Discussion

In this section, the effects of different system parameters on the vibration characteristics of the rotor system are analyzed. The critical parameters in the equations governing the vibrations of the linear system (Eq. (12) with $\lambda = 0, \nu = 0$) are: internal damping factor (μ_i), damping factors (μ_x, μ_z), undamped natural frequencies (ω_x, ω_z), gyroscopic coefficient (G), the amplitude of excitation ($q_0 = \gamma r_e r_f^2$), and the effective mass (m_e). Damping factors (μ_x, μ_z) are functions of the external damping coefficients (c_{ex}, c_{ez}), internal damping coefficient (μ_i), and the damping coefficients of the bearings (c_1, c_2). These parameters depend on other system parameters, like the eccentricity ratio (r_e), mass ratio (r_m), mass moment of inertia of the disc about x-axis (r_{dx}), polar moment of the disc about y-axis (r_{dy}), radius of gyration (r), end spring stiffness (k_{11}, k_{21}), etc. Henceforth, for convenience, the first set of parameters ($\omega_x, \omega_z, G, q_0, m_e, \mu_x, \mu_z, \mu_i$) will be called as the dependent parameters and the second set of parameters ($c_1, c_2, c_{ex}, c_{ez}, c_i, r_e, r_m, r_{dx}, r_{dy}, r, k_{11}, k_{21}$) as the independent parameters. Moreover, the system dynamics are also affected by the gyroscopic effects of the disc and shaft associated with the terms D_g and S_g , respectively, and the rotary inertia of the disc and shaft associated with the terms D_r and S_r , respectively.

A set of independent parameters listed in Table 1 are used in the forthcoming analysis. Most of these parameters are taken from the references [13–15, 23–26, 39, 43]. Independent parameters different from these values are specified at the caption of each figure. In most of the cases, the

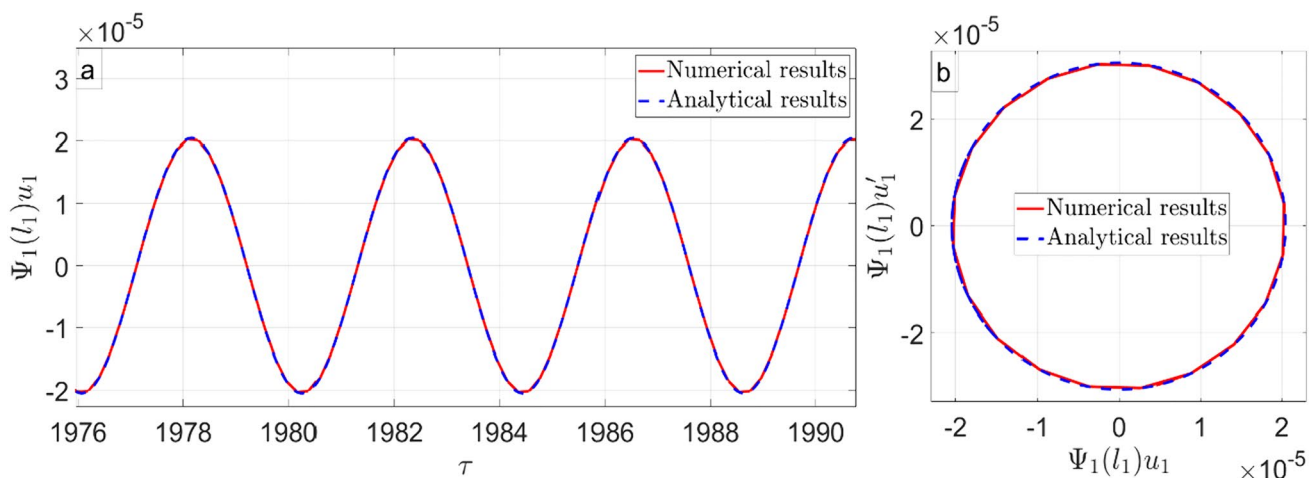


Fig. 3 Time response and phase plane plots in horizontal direction. Parameters: Table 1, $c_i = 0.0000085$, and $l_1 = 0.2$

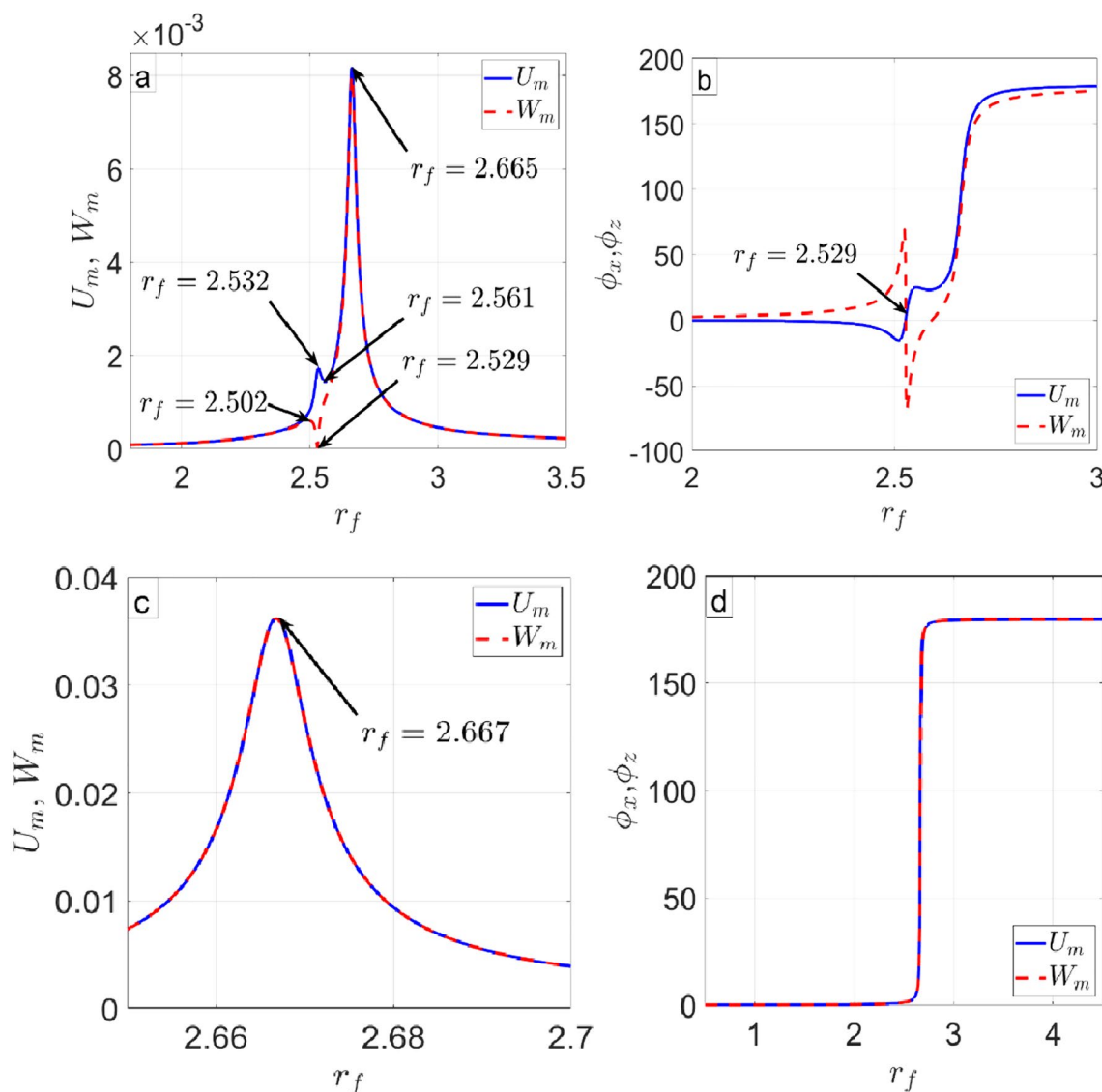


Fig. 4 Frequency response and phase angle plots in horizontal and vertical direction. Parameters: **a, b** Table 1 and $l_1 = 0.3, c_{ez} = 0.085, c_2 = 0.02$, **c, d** Table 1, $c_{ex} = c_{ez} = 0.0085$ and $l_1 = 0.3$

system dynamics are analyzed from the frequency response diagrams and phase angle plots. In frequency response diagrams, the amplitude of oscillation at the middle of the shaft ($U_m = \Psi_1(0.5)U_1, W_m = \Psi_1(0.5)W_1$) is plotted with respect to the dimensionless frequency (r_f). For the set of parameter values chosen for this work, the maximum deflection at the middle of the shaft is restricted below 0.1 times the length of the shaft. This is considered as the small deflection criterion for the present study. The maximum deflection can further be reduced by selecting the eccentricity ratio (r_f) appropriately without compromising the qualitative results of the rotor system. Based on the small deflection criterion, the nonlinearities in the rotor system can be neglected.

The analytical expressions derived for the horizontal and vertical displacements (Eqs. (16)) are verified by comparing the time-displacement and phase-plane plots obtained from Eqs. (16) with those obtained from the numerical simulation of the governing Eqs. (14). For both the horizontal and vertical oscillations, the analytical results match exactly with the numerical results. The horizontal direction results are presented shown in Fig. 3.

In most of the literatures on rotor dynamics, the damping along horizontal and vertical directions ($\mu_x = \mu_z = \mu$) are considered to be the same [22, 23, 28, 43]. Some researchers, though, analyzed the effect of different amount of damping ($\mu_x \neq \mu_z$) on the vibrations of rotor system [39]. As the bearings are considered to be isotropic in this study, the

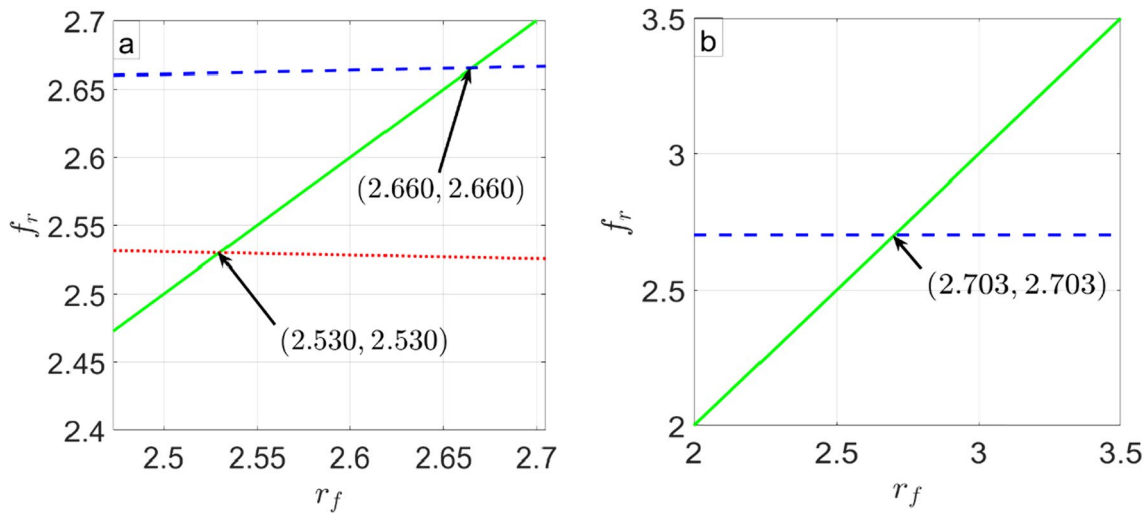


Fig. 5 Campbell diagrams **a** corresponding to the plots in Fig. 4a and b, **b** corresponding to the plots in Fig. 4c, d

Table 2 Values of dependent parameters for different values of independent parameters

Figs. no.	Independent Parameters	Dependent Parameters						
		G	ω	m_e	$\mu_x = \mu_z$	$q_0 \times 10^{-4}$	$(r_f)_r$	$U_p = W_p$
6	$r_m = 0.5$	-0.415	7.324	1.537	0.00613	29.51	7.311	0.0554
	$r_m = 0.8$	-0.504	8.761	2.040	0.00474	32.04	8.769	0.0662
	$r_m = 1.2$	-0.572	10.04	2.697	0.00352	34.15	10.04	0.076
7a	$r = 0.1$	-0.053	2.667	1.440	0.00665	5.634	2.667	0.0362
	$r = 0.2$	-0.089	2.694	1.467	0.00653	5.643	2.694	0.0365
	$r = 0.3$	-0.147	2.741	1.513	0.00633	5.665	2.741	0.0372
7b	$r_{dx} = 0.05$	-0.053	2.667	1.440	0.00665	5.635	2.666	0.0362
	$r_{dx} = 0.08$	-0.052	2.650	1.457	0.00657	5.497	2.651	0.0357
	$r_{dx} = 0.12$	-0.051	2.628	1.480	0.00647	5.321	2.627	0.0356
8a	$k_{21} = 100$	-0.0087	2.239	1.899	0.00681	3.531	2.237	0.0030
	$k_{21} = 500$	-0.0089	2.189	2.042	0.00095	3.262	2.186	0.0217
	$k_{21} = 6000$	-0.0091	2.178	2.071	0.00069	3.207	2.177	0.0294
8b	$l_1 = 0.2, 0.8$	-0.144	3.569	0.890	0.0107	12.19	3.569	0.0270
	$l_1 = 0.3, 0.7$	-0.053	2.667	1.440	0.00665	5.635	2.667	0.0362
	$l_1 = 0.5$	-0.008	2.189	2.042	0.00469	3.262	2.189	0.0441
9a	$D_g = 1, S_g = 1$	-0.0530	2.667	1.440	0.00665	5.635	2.667	0.0362
	$D_g = 1, S_g = 0$	-0.040	2.649	1.440	0.00665	5.559	2.649	0.0359
	$D_g = 0, S_g = 1$	-0.012	2.612	1.440	0.00665	5.405	2.612	0.0354
	$D_g = 0, S_g = 0$	0	2.595	1.440	0.00665	5.335	2.595	0.0351
9b	$D_r = 1, S_r = 1$	-0.0530	2.667	1.440	0.00665	5.635	2.667	0.0362
	$D_r = 0, S_r = 1$	-0.0534	2.676	1.410	0.00679	5.790	2.676	0.0363
	$D_r = 1, S_r = 0$	-0.0540	2.696	1.430	0.00670	5.795	2.696	0.0365
	$D_r = 0, S_r = 0$	-0.0545	2.705	1.401	0.00684	5.955	2.705	0.0367

only source of difference in damping is to consider two different values for external damping coefficients ($c_{ex} \neq c_{ez}$). It is explained in the section "Exact Analytical Solution and Analysis of Free Vibrations" how in the special case of equal damping ($\mu_x = \mu_z = \mu$), the two equations along the horizontal and vertical directions (Eq. (12) with $\lambda = 0$,

$v = 0$) are written as a single equation (Eq. (21)) in terms of a complex variable. This shows that the system responses along horizontal and vertical directions will differ only in case of different amount of damping ($\mu_x \neq \mu_z$) along these two directions. For the choice of equal amount of damping ($\mu_x = \mu_z = \mu$), the system becomes isotropic and the system

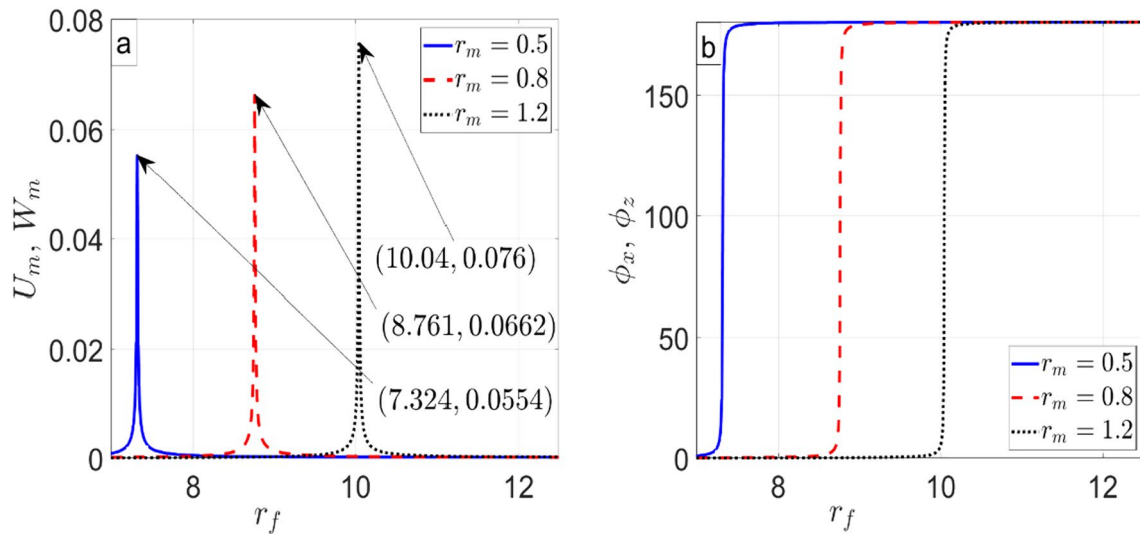


Fig. 6 a Frequency response plots, and b Phase angle plots for different values of r_m . Parameters: Table 1, $c_{ex} = c_{ez} = 0.0085$, and $l_1 = 0.2$

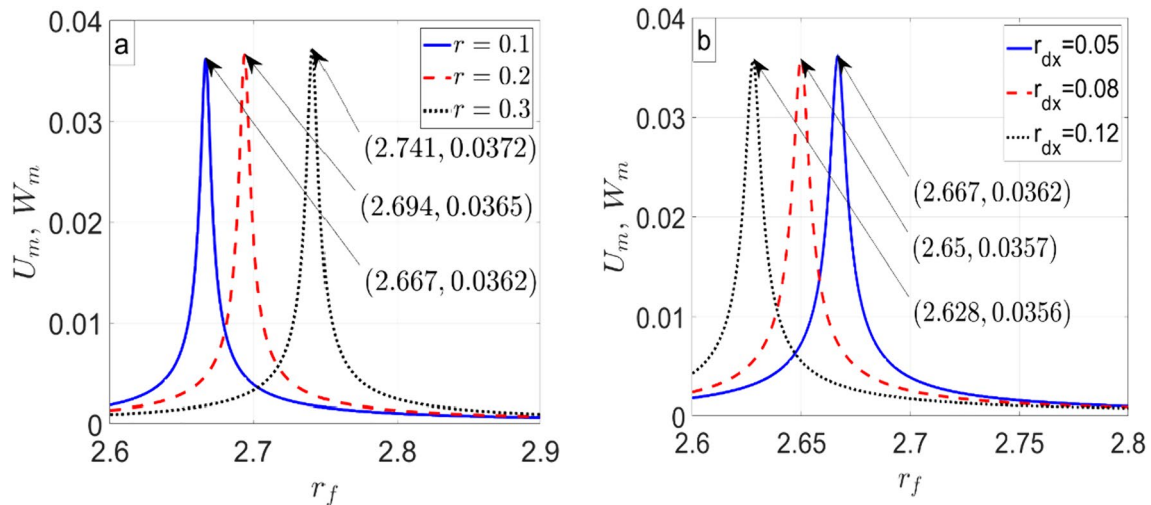


Fig. 7 Frequency response plots for different values of r and r_{dx} . Parameters: Table 1, $c_{ex} = c_{ez} = 0.0085$, and $l_1 = 0.3$, a $r_{dx} = 0.05$, b Table 1

dynamics along these two directions become identical. This is verified from the frequency response diagrams and phase angle plots in Figs. 4.

The two peaks in the frequency response diagram for different amount of damping along the horizontal and vertical directions ($\mu_x = 0.00106$, $\mu_z = 0.0594$) are marked in Fig. 4a. These resonance frequencies are further verified from the Campbell diagram plotted in Fig. 5a. To plot this Campbell diagram, Eq. (20) is first solved for β for different values of excitation frequency r_f . The imaginary part of β is the damped natural frequency f_r , which is plotted in Fig. 5a with respect to r_f . The higher damping along vertical direction causes a noticeable reduction in peak

amplitude of oscillations at second resonance frequency $r_f = (r_f)_{r2} = 2.665$.

The phase angle ϕ_z for horizontal oscillations changes suddenly from positive to negative near the first resonance frequency $(r_f)_{r1}$ as shown in Fig. 4b. Contrary to that, the sudden change in phase angle ϕ_x for vertical oscillations is from negative to positive near $(r_f)_{r1}$. The amplitude of oscillations and phase angles along horizontal and vertical directions become indistinguishable for same amount of damping ($\mu_x = \mu_z = 0.0066$) as shown in Fig. 4c and d. Moreover, only one resonance peak is observed from the frequency response diagram. The presence of single resonance frequency is further verified from the Campbell diagram shown in Fig. 5b.

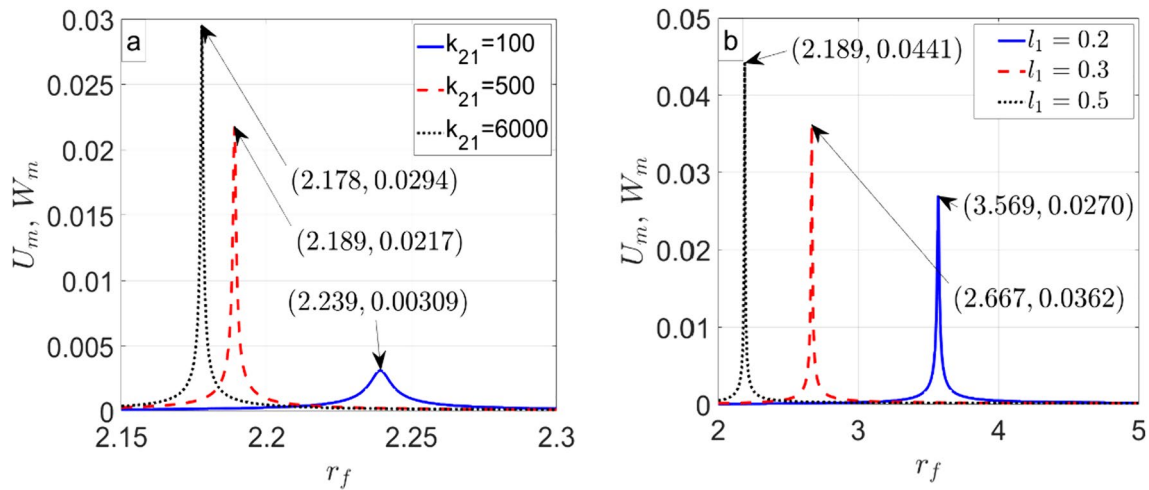


Fig. 8 Frequency response plots for different values of k_{21} and l_1 . Parameters: $c_{ex} = c_{ez} = 0.0085$, **a** $l_1 = 0.5$, and **b** Table 1

Equal amount of damping ($c_{ex} = c_{ez}$, $c_1 = c_2$) is considered for the forthcoming analysis wherein the effect of other system parameters on the dynamics of the rotor system is studied through frequency response and phase angle plots. As the vibration characteristics along horizontal and vertical directions become identical for equal amount of damping, only one set of results are plotted.

The values of the dependent parameters (ω_x , ω_z , G , q_0 , m_e , μ_x , μ_z , μ_i) as well as the damped natural frequency (resonance frequency (r_f)) associated with rest of the figures are listed in Table 2 for effective analysis of the results.

The amplitude-frequency and phase angle plots for different values of mass ratio r_m ($= \rho AL/M_d$) are shown in Fig. 6. It is observed from Fig. 6 that the system resonant frequency increases with the increase of r_m . Also, the peak amplitude at resonance increases with the increase of r_m . It is noticed from the values of different parameters listed in Table 2 that the effective mass m_e of the system is larger for higher values of r_m . However, the magnitude of the gyroscopic coefficient G , the undamped natural frequency ω and amplitude of excitation q_0 increases with the increase of r_m , even though m_e appears in the denominator of the expressions of G , ω and q_0 (Eqs. (13c) and (13d)). This results in higher values of the damped natural frequency (r_f) of the system as the value of r_m is increased. The expression for μ ($= \mu_x = \mu_z$) are inversely proportional to m_e (Eqs. (13a) and (13b)) and consequently, their values decrease with the increase of r_m . This results in higher values of peak amplitude at resonance at higher values of r_m and q_0 is increases with the increase of r_m . Physically, the higher values of r_m causes the system stiffness to increase causing the damped natural frequency to increase and the peak amplitude at resonance increases due to reduction in damping factor μ . The asymptotic values of

the phase angle (ϕ) are 0° and 180° as $r_f \rightarrow 0$ and $r_f \rightarrow \infty$, respectively, with the sharp change in ϕ happening near the resonance frequency as shown in Fig. 6b. In all the forthcoming analysis, the nature of phase angle plots is similar to Fig. 6b. As, no new information is obtained from the phase angle plots, they are not included for the subsequent analysis.

The effect of the radius of gyration r (dimensionless) of the shaft cross-section on the system response is shown in Fig. 7a. Exactly as in the case of mass ratio r_m , the values of the parameters $|G|$ (magnitude of G), ω , q_0 , and m_e increase and the values of the parameters μ_x , and μ_z decrease with the increase of r . The qualitative nature of the frequency–response curves for different values of r shown in Fig. 7a which is similar to Fig. 6a plotted for different values of r_m ; the resonance frequency and the peak amplitude at resonance increase as the value of r is increased. The damping factors have more influence on the peak amplitude at resonance than the excitation amplitude q_0 .

The impact of the dimensionless mass moment of inertia of the disc about x -axis ($r_{dx} = I_{dx}/\rho AL^3$) on the frequency response curves is shown in Fig. 7b. The parameter r_{dx} appear in the expression for m_e given by Eq. (13c). With increasing r_{dx} , the value of the parameter m_e increases which results in lower magnitudes of G , ω , μ_x , μ_z and q_0 . As an outcome, the resonance frequency as well as the peak amplitude at resonance reduces for higher values of r_{dx} as shown in Fig. 7b. The influence of r_{dx} is contrary to the trend revealed by mass ratio r_m and radius of gyration r as shown in Figs. 6a and 7a.

The bearings at the end of the shaft are replaced by linear springs and damper (Kelvin–Voigt model) along horizontal

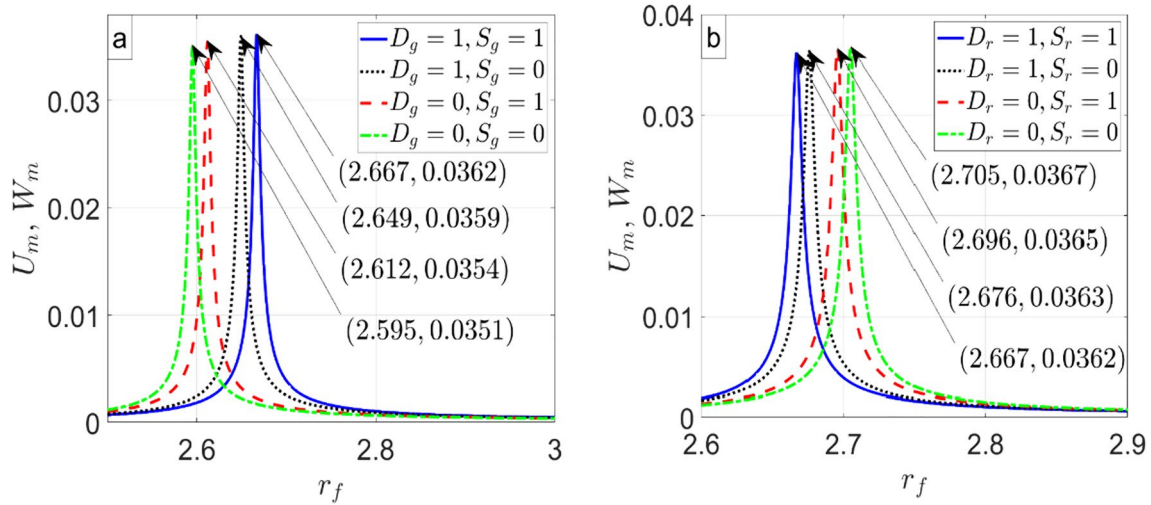


Fig. 9 Frequency response plots for different values of D_g, S_g, D_r & S_r . Parameters: Table 1 and $l_1 = 0.3$. **a** $D_r = S_r = 1$, **b** $D_g = S_g = 1$

and vertical directions. They directly influence the mode shape Ψ_1 shown in Fig. 2 as well as the natural frequency p_1 . Other parameters of the rotor system governed by Eq. (14) are influenced through Ψ_1 and p_1 . Figure 8a depicts the influence of the support spring stiffness k_{21} on the frequency response plots. The stiffness of left-end bearing (bearing B_1) is kept constant at $k_{11} = 500$ while obtaining the three frequency response curves for three different values of k_{21} in Fig. 8a. The overall stiffness of the system decreases for higher values of k_{21} resulting in lower resonant frequencies. The excitation amplitude q_0 and the damping factor μ decrease with the increase of k_{21} (Table 2) yielding the peak amplitude at resonance to increase as shown in Fig. 8a. It is to be mentioned here that the right-end bearing (bearing B_2) can be considered a rigid one for $k_{21} = 6000$. When

$k_{11} = k_{21} = 100$, the mode shape is symmetric about $l_1 = 0.5$ (refer Fig. 2). As the disc is installed at the middle of the shaft ($l_1 = 0.5$), the gyroscopic parameter $G = -0.0089$ in Table 2 for $k_{11} = k_{21} = 500$ is entirely due to the gyroscopic effect of the shaft. As the stiffness of bearing B_2 is increased, the symmetry of the mode shape about $l_1 = 0.5$ is lost. The gyroscopic effect of the disc increases with the increase of k_{21} which is manifested in the increasing value of $|G|$. Maximum value of $|G|$ is achieved for a rigid bearing at B_2 .

Figure 8b depicts the effect of l_1 on the frequency response and phase angle plots. The parameter l_1 specifies the position of the disc from left-end of the support (from bearing B_1). If the disc is at the center of the shaft ($l_1 = 0.5$), the gyroscopic and rotary inertia effects of the disc associated with the terms D_g and S_g , respectively, are zero

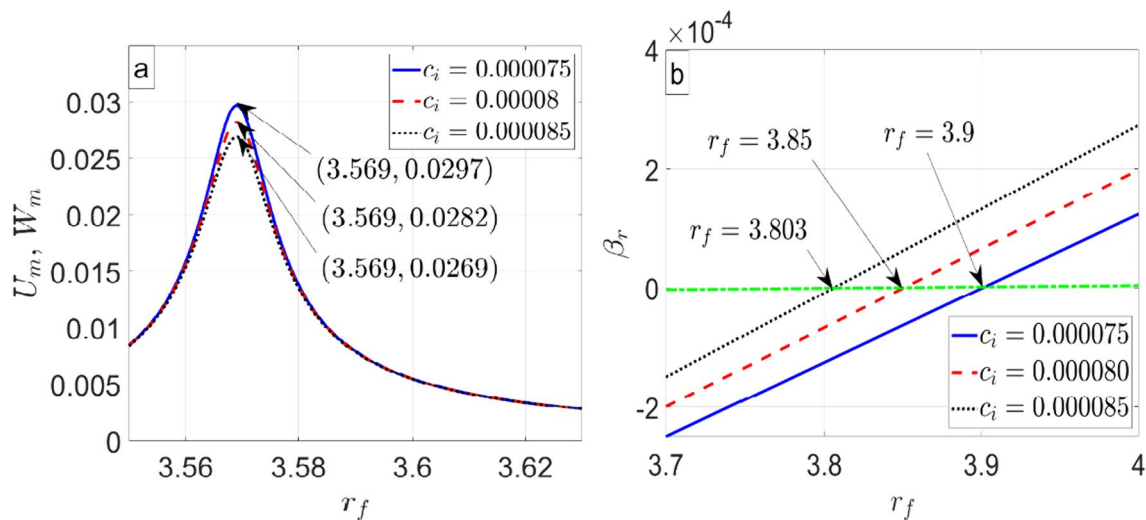


Fig. 10 **a** Frequency response and **b** β_r versus r_f for different values of c_i . Parameters: Table 1, and $l_1 = 0.2$

Table 3 Parameter values for different values of internal damping coefficient

Fig. no.	Control parameters	G	ω	m_e	$\mu_x = \mu_z$	μ_i	$q_0 \times 10^{-4}$	$(r_f)_r$	$(r_f)_c$	$U_p = W_p$
10	$c_i = 0.000075 - 0.144$	3.569	0.890	0.00977	0.00759	12.19	3.569	3.900	0.0297	
	$c_i = 0.00008 - 0.144$	3.569	0.890	0.01020	0.00810	12.19	3.569	3.850	0.0282	
	$c_i = 0.000085 - 0.144$	3.569	0.890	0.01071	0.00861	12.19	3.569	3.803	0.0269	

$(D_g r_{dy} r_m(t_5 - t_6) = 0, D_{ri} r_{dx} r_m(t_5 - t_6) = 0)$. This leads to the largest effective mass ratio ($m_e = 2.042$) and smallest magnitude of gyroscopic coefficient ($|G| = 0.008$) for $l_1 = 0.5$ as shown in Table 2. The value of the gyroscopic coefficient ($G = -0.008$) is entirely due to the gyroscopic effect of the shaft. The final consequence is the lowest resonance frequency for $l_1 = 0.5$ as shown in Fig. 8b. As the disc is moved away from the middle of the shaft and towards one of the bearing supports (l_1 is either decreased or increased), the magnitude of G is increased and m_e is decreased leading to higher values of resonance frequencies. Because of the symmetry of the mode shape function $\Psi_1(y)$ about $y = 0.5$, the frequency response curves would be identical for $l_1 = 0.3$ and $l_1 = 0.7$ (or $l_1 = 0.2$ and $l_1 = 0.8$). This can also be explained mathematically. In the expressions for m_e and G given by Eqs. (13c) and (13d), respectively, all the terms except $t_5 - t_6 = -\left(\frac{d\Psi_1}{dy}\right)^2 \Big|_{y=l_1}$ and $t_4 = \Psi_1^2(l_1)$ remain the same while l_1 is varied. Now, because of the symmetry of the

curve $\Psi_1(y)$ about $y = 0.5$, $\left(\frac{d\Psi_1}{dy}\right)^2 \Big|_{y=0.3} = \left(\frac{d\Psi_1}{dy}\right)^2 \Big|_{y=0.7}$, and $\Psi_1^2(0.3) = \Psi_1^2(0.7)$. Consequently, the magnitudes of m_e and G will be the same leading to the identical frequency response curves for $l_1 = 0.3$ and $l_1 = 0.7$. As the disc approaches the support, the values of q_0 , μ_x , μ_z , and μ_m drop, which causes the amplitude peaks to decrease.

The influence of disc and shaft gyroscopic effects is illustrated in Fig. 9a. It is mentioned earlier that the terms associated with D_g and S_g are the gyroscopic effects of the disc and the shaft, respectively. The gyroscopic coefficient $G = 0$ when both these effects are neglected ($D_g = S_g = 0$). The consequence is the lowest resonance frequency as shown in Fig. 9a. On the other hand, the magnitude of G ($= 0.0530$) as well as the resonance frequency is the maximum for $D_g = S_g = 1$. The effective mass m_e is independent of the gyroscopic terms. Consequently, the resonance frequency $(r_f)_r$ and the amplitude of excitation q_0 remains unaltered. However, the damping factor μ remains the same for all the

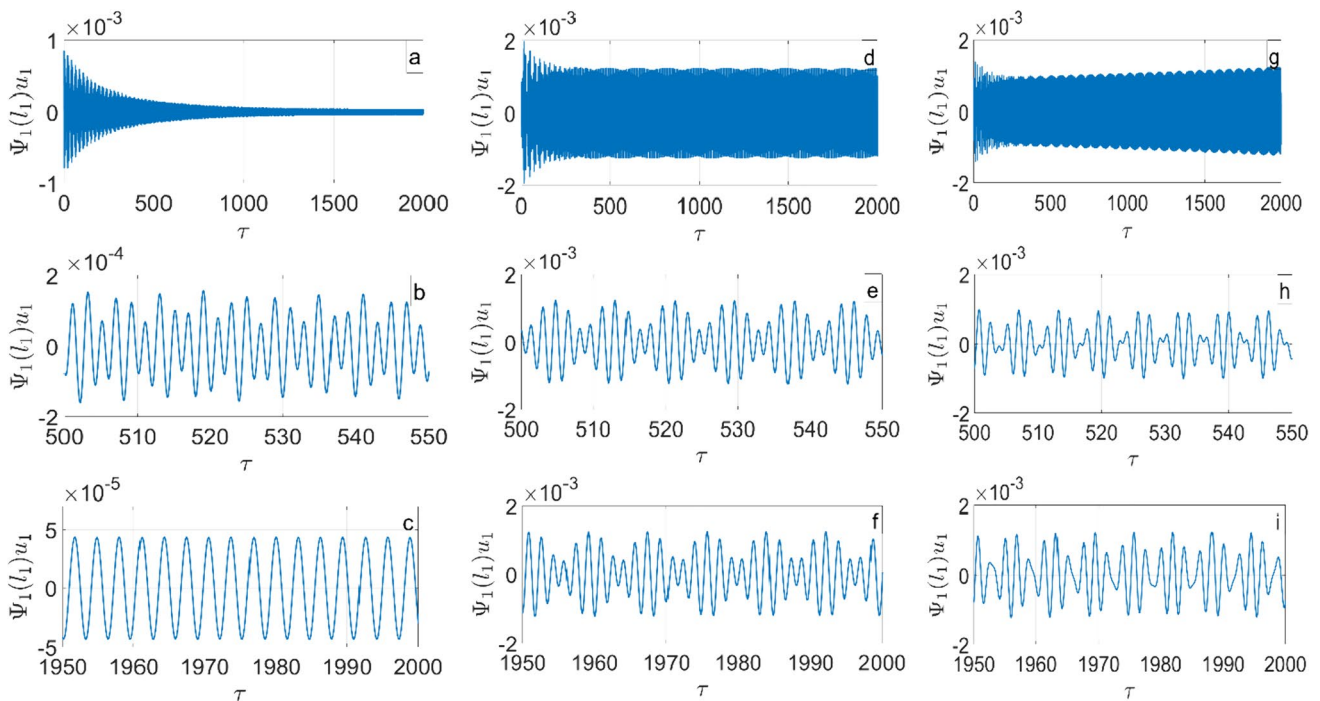


Fig. 11 Time responses for different values of r_f . Parameters: Table 1, $\mu_i = 0.000085, l_1 = 0.2$, **a-c** $r_f = 2.5$, **d-f** $r_f = 3.806$ and **g-i** $r_f = 4$

values of D_g and S_g . The outcome is the higher resonance frequency and the peak amplitude at resonance for higher values of the gyroscopic coefficient. The gyroscopic effect of the shaft appears to have a greater influence in increasing the resonance frequency and peak amplitude at resonance compared to the gyroscopic effect of the disc.

Figure 9b shows the effect of disc and shaft rotary inertia effects (D_r and S_r) on the rotor system responses (amplitude and phase angle). The rotary inertia terms associated with D_r and S_r appear in Eq. (13c) in the expression of effective mass m_e . It is to be noticed from Eq. (13) that the excitation amplitude q_0 , gyroscopic coefficient G , and undamped natural frequency ω are all inversely proportional to m_e . In absence of the rotary inertia effects of the disc and shaft ($D_r = S_r = 0$), the value of m_e ($= 1.401$) is the lowest and the magnitude of G is the highest. This leads to the highest resonance frequency as shown in Fig. 9b. Furthermore, q_0 is found to be the highest ($= 5.955$) resulting in highest peak amplitude at resonance for $D_r = S_r = 0$. On the other hand, highest value of m_e and lowest magnitude of G are obtained for $D_r = S_r = 1$. This leads to the lowest resonance frequency for $D_r = S_r = 1$. Lowest excitation amplitude q_0 results in the lowest peak amplitude of oscillation at resonance for $D_r = S_r = 1$. As in the case of gyroscopic effects, the shaft rotational inertia has greater influence in increasing the resonance frequency in comparison to the disc rotational inertia.

It is to be noted that all the aforementioned results are obtained without any internal damping ($c_i = 0$). It is shown in the section "Exact Analytical Solution and Analysis of Free Vibrations" that the response of the rotor system is always stable for $c_i = 0$. However, a small amount of internal damping may cause instability of system response for frequency ratios beyond a critical value ($r_f \geq (r_f)_c$). This is verified in the forthcoming analysis.

The three frequency response curves shown in Fig. 10a are plotted for three difference values of internal damping coefficients. For effective analysis of the influence of internal damping on the system responses, the dependent parameters are listed in Table 3. It is observed from Table 3 that the gyroscopic parameter (G), undamped natural frequency (ω), effective mass ratio (m_e), amplitude of excitation (q_0), and the resonance frequency ($(r_f)_r$) are all independent of c_i . However, the damping factor μ ($= \mu_x = \mu_z$), and the internal damping factor μ_i increases with the increase of c_i . This causes the peak amplitude at resonance to decrease with the increase of c_i as shown in Fig. 10a. The range of frequencies corresponding to the stable solutions decreases with the increase of c_i . This is evident from the decreasing value of $(r_f)_c$ with the increase of c_i . These critical values of r_f separating the stable and unstable solutions for free vibrations are further verified by plotting the real part of the roots (β_r) with respect to r_f . This plot is shown in Fig. 10b which

depicts the change of sign of β_r from negative to positive as the frequency ratio r_f is increased beyond the critical value $(r_f)_c$. Clearly, the homogeneous solution of Eq. (14) is stable for $r_f \leq (r_f)_c$ and unstable for $r_f > (r_f)_c$.

The responses of the rotor system (Eq. (14)) in the stable region ($r_f < (r_f)_c$), unstable region ($r_f > (r_f)_c$), and at the stability boundary ($r_f = (r_f)_c$) are investigated in Fig. 11 for $c_i = 0.000085$. The critical frequency ratio corresponding to $c_i = 0.000085$ is $(r_f)_c = 3.806$. The time-displacement response of Eq. (14) for $r_f = 2.5 < (r_f)_c$ is shown in Fig. 11a. This is a combination of homogeneous and particular solutions of Eq. (14). The frequencies of homogeneous and particular solutions superimpose causing the modulation at the initial phase as shown in Fig. 11b. As $\beta_r < 0$, the homogeneous solution die out over time yielding a single periodic motion corresponding to the particular solution as shown in Fig. 11c. Since $\beta_r = 0$ for $r_f = 3.803 = (r_f)_c$, the homogeneous solution never dies out. Consequently, the time-response of the system is always modulated as shown in Fig. 11d–f. However, the mean amplitude of oscillations will remain constant at steady state. On the other hand, the mean amplitude of oscillation increases unboundedly for $r_f = 4 > (r_f)_c$ as shown in Fig. 11g–i. This homogeneous solution is unstable for $r_f = 4$ because of positive value of β_r . This causes the unbounded time-displacement response of the rotor system depicted in Fig. 11g–i.

Conclusion

A systematic investigation of a continuous rotor model was performed in this paper to analyse the effect of different parameters on the natural frequency and stability of the system. The rotor system was modelled with the inclusion of several critical factors like the rotary inertia and gyroscopic effects of both shaft and disc, internal damping, large deformation of shaft, and restriction to shaft axial motion. The bearings on the two sides of the shaft were considered to be isotropic and were replaced by spring-dashpot systems along horizontal and vertical directions. The PDEs governing the system vibrations, derived from Hamilton's Principle, were reduced to a set of ODEs using the method of modal projection. As the paper is mainly focused in exploring the effect of different system parameters on the resonance frequency, only the linear system was analysed.

The effect of various independent parameters on the nature of vibrations of the linear rotor system were analyzed both numerically and analytically. These independent parameters are associated to the material and geometrical properties of the rotor system and connected to

the governing ODEs through the effective mass ratio (m_e) and gyroscopic coefficient (G). The dependent parameters, tabulated as functions of the independent parameters, were used for the effective analysis of the results. This methodical analysis, which connects the system dynamics to the material and geometric properties of the rotor system, could result in a suitable design.

The system becomes isotropic with identical responses along horizontal and vertical directions for equal amount of damping along these directions. The resonant frequency was observed to increase with the increase of mass ratio (r_m), radius of gyration (r), and the end spring stiffness (k_{11} , k_{21}). On the other hand, the resonance frequency decrease with the increase of the mass moment of inertia of the disc about x -axis (r_{dx}). While the gyroscopic effects of the disc and shaft tend to increase the resonance frequency, the rotary inertia of the disc and shaft tend to decrease the resonance frequency.

The stability of the rotor system mainly depends upon the internal damping parameter (μ_i). A strain rate dependent internal damping model was used in this paper. Analytical expression for a critical frequency ratio ($(r_f)_c$) corresponding to the stability boundary separating the stable and unstable regions was obtained. This critical value of r_f was further verified by analysing the time responses of the rotor system for $r_f < (r_f)_c$, $r_f = (r_f)_c$, and $r_f > (r_f)_c$. For $r_f < (r_f)_c$, the response was observed to reach a single periodic steady-state over time. A modulating time response was obtained for $r_f = (r_f)_c$. This is the consequence of superposition of homogeneous and particular solutions. For $r_f > (r_f)_c$, the system is unstable and the time-response grows monotonically.

There is a lot of scope to extend the present work. The rotor system with nonlinearities arising from the large deformation of shaft, restriction to shaft axial motion, and nonlinear spring in place of bearings can be considered for future analysis. The feasibility of getting a same/different solution with nonlinear springs at the supports showing force–deflection relations similar to the Hertzian contact at ball bearings can be examined in future. One may try to derive a different mode shape function from a different set of boundary conditions obtained from the boundary terms which appear during the application of the Hamilton's principle. Another scope for future work could be the use of hydrodynamic bearings instead of ball bearings.

Acknowledgements This work has been supported by Startup Research Grant (SRG) funded by DST-SERB under Project File no. SRG/2019/001445 and National Institute of Technology Calicut under Faculty Research Grant. We are also grateful to Dr. M. D. Narayanan for his support and advice.

Author Contributions All authors contributed to the study conception and design. Material preparation, data collection and analysis were performed by Amit Malgol, Vineesh K P and Ashesh Saha. The first

draft of the manuscript was written by Amit Malgol and all authors commented on previous versions of the manuscript. All authors read and approved the final manuscript.

Funding This work has been supported by DST SERB—SRG under Project File no. SRG/2019/001445 and National Institute of Technology Calicut under Faculty Research Grant. We are also grateful to Dr. M. D. Narayanan for his support and advice.

Data Availability The datasets generated during and/or analysed during the current study are not publicly available due to ongoing research or future publications but are available from the corresponding author on reasonable request.

Declarations

Conflict of Interest Financial interests: The authors have no relevant financial or non-financial interests to disclose. The authors declare that they have no conflict of interest.

References

- Nayfeh AH (1993) Introduction to perturbation techniques. Wiley, New York
- Meirovitch L (1997) Principles and techniques of vibrations. Prentice Hall
- Michel L, Guy F (1998) Rotor dynamics prediction in engineering, 2nd edn. Wiley
- Ghosh A, Mallik AK (2015) Theory of mechanisms and machines. Affiliated East West Press, New Delhi
- Yukio I, Toshio Y (2012) Linear and nonlinear rotordynamics: a modern treatment with applications. Wiley
- Shaw J, Shaw S (1989) Instabilities and bifurcations in a rotating shaft. *J Sound Vib* 132(2):227–244
- Shaw J, Shaw S (1991) Non-linear resonance of an unbalanced rotating shaft with internal damping. *J Sound Vib* 147(3):435–451
- Azeez MFA, Vakakis AF (1999) Numerical and experimental analysis of a continuous overhung rotor undergoing vibro-impacts. *Int J Non-Linear Mech* 34(3):415–435
- Duchemin M, Berlioz A, Ferraris G (2006) Dynamic behavior and stability of a rotor under base excitation. *J Vib Acoust Trans ASME* 128(5):576–585
- Pavlović R, Kozić P, Mitić S, Pavlović I (2009) Stochastic stability of a rotating shaft. *Arch Appl Mech* 79:1163–1171
- Phadatare HP, Pratihari B (2020) Dynamic stability and bifurcation phenomena of an axially loaded flexible shaft-disk system supported by flexible bearing. *Proc IMech Part C: J Mech Eng Sci* 234(15):2951–2967
- Diken H, Alnefaie K (2011) Effect of unbalanced rotor whirl on blade vibrations. *J Sound Vib* 330:3498–3506
- Shad MR, Michon G, Berlioz A (2011) Modeling and analysis of nonlinear rotor dynamics due to higher order deformations in bending. *Appl Math Model* 35:2145–2159
- Shad MR, Michon G, Berlioz A (2011) Analytical study of the dynamic behavior of geometrically nonlinear shaft-disk rotor systems. *Mech Ind* 12:433–443
- Shad MR, Michon G, Berlioz A (2012) Nonlinear dynamics of rotors due to large deformations and shear effects. *Appl Mech Mater* 110(116):3593–3599
- Khanlo HM, Ghayour M, Ziaei-Rad S (2012) Disk position non-linearity effects on the chaotic behaviour of rotating flexible shaft-disk systems. *J Mech* 28(3):513–522

17. Li W, Sheng D, Chen J, Che Y (2014) Modeling a two-span rotor system based on the Hamilton principle and rotor dynamic behaviour analysis. *J Zhejiang Univ Sci A* 15:883–895
18. Yongsheng R, Xingqi Z, Yanghang L, Xiulong C (2014) An analytical model for dynamic simulation of the composite rotor with internal damping. *J of Vibroengineering* 16(8):4002–4016
19. Varanis M, Mereles A, Silva A, Balthazar JM, Tusset ÂM (2018) Rubbing effect analysis in a continuous rotor model. In: *Proceedings of the 10th international conference on rotor dynamics – IFToMM*, pp 387–399
20. Deb F, Jegadeesan K, Shrivankumar C (2018) Analysis of a rotor supported in bearing with gyroscopic effects. *IOP Conf Ser Mater Sci Eng* 402:012059
21. Kim J, Hong JG, Chung J (2019) Nonlinear dynamic modeling and response analysis of a rotor–blade system with whirling motion. *Nonlinear Dyn* 98:953–970
22. Malgol A, Saha A (2022) Influence of gyroscopic effect and rotary inertia on the vibrations of a continuous rotor system. In: *Popat KC, Kanagaraj S, Sreekanth PSR, Kumar VMR (eds) Advances in mechanical engineering and material science: ICAMEMS 2022—lecture notes in mechanical engineering*. Springer, Singapore
23. Mukherjee A, Rastogi V, Dasgupta A (2009) Extension of Lagrangian–Hamiltonian mechanics for continuous systems—investigation of dynamics of a one-dimensional internally damped rotor driven through a dissipative coupling. *Nonlinear Dyn* 58:107–127
24. Samantaray AK, Dasgupta SS, Bhattacharyya R (2009) Bond graph modeling of an internally damped nonideal flexible spinning shaft. *J Dyn Syst Meas Control* 132:1–9
25. Dasgupta SS, Rajamohan V (2017) Dynamic characterization of a flexible internally damped spinning shaft with constant eccentricity. *Arch Appl Mech* 87:1769–1779
26. Dasgupta SS, Samantaray AK, Bhattacharyya R (2010) Stability of an internally damped non-ideal flexible spinning shaft. *Int J Non Linear Mech* 45(3):286–293
27. Phadatare HP, Pratiher B (2020) Nonlinear modeling, dynamics, and chaos in a large deflection model of a rotor–disk–bearing system under geometric eccentricity and mass unbalance. *Acta Mech* 231:907–928
28. Shih YS, Wu GY, Chen EJS (1998) Transient vibrations of a simply-supported beam with axial loads and transverse magnetic fields. *Mech Struct Mach Int J* 26(2):115–130
29. Greenhill LM, Cornejo GA (1995) Critical speeds resulting from unbalance excitation of backward whirl modes. *Am Soc Mech Eng Des Eng Div* 84(2):991–1000
30. Luczko J (2002) A geometrically nonlinear model of rotating shafts with internal resonance and self-excited vibrations. *J Sound Vib* 255(3):433–456
31. Ishida Y, Inoue T (2004) Internal resonance phenomena of the Jeffcott rotor with nonlinear spring characteristics. *J Vib Acoust Trans ASME* 126(4):476–484
32. Cveticanin L (2005) Free Vibration of a Jeffcott rotor with pure cubic non-linear elastic property of the shaft. *Mech Mach Theory* 40:1330–1344
33. Dimentberg MF, Naess A (2008) Nonlinear vibrations of a rotating shaft with broadband random variations of internal damping. *Nonlinear Dyn* 51:199–205
34. Hosseini S, Khadem S (2009) Free vibration analysis of a rotating shaft with nonlinearities in curvature and inertia. *Mech Mach theory* 44:272–288
35. Samantaray AK (2009) Steady-state dynamics of a non-ideal rotor with internal damping and gyroscopic effects. *Nonlinear Dyn* 56:443–451
36. Cveticanin L (1995) Resonant vibrations of nonlinear rotors. *Mech Mach Theory* 30(4):581–588
37. Boyaci A, Lu D, Schweizer B (2014) Stability and bifurcation phenomena of Laval/Jeffcott rotors in semi-floating ring bearings. *Nonlinear Dyn* 79:1535–1561
38. Jahromi AF, Bhat RB, Xie WF (2015) Forward and backward whirling of a rotor with gyroscopic effect. In: *Sinha JK (ed) Vibration engineering and technology of machinery, mechanisms and machine science*, vol 23. Springer, Switzerland, pp 879–887
39. Saeed NA, El-Gohary HA (2016) On the nonlinear oscillations of a horizontally supported Jeffcott rotor with a nonlinear restoring force. *Nonlinear Dyn* 88(1):1–22
40. Matsushita O, Tanaka M, Kanki H, Kobayashi M, Keogh P (2017) Gyroscopic effect on rotor vibrations. *Mathematics for Industry*. Springer, Tokyo, pp 153–180
41. Mittal RK, Kulkarni SS, Singh RK (2018) Multiple degree of freedom rotordynamics of stability modeling in high-speed micro-milling of Ti-6Al-4V. *Procedia Manuf* 26:607–616
42. Ali A, Hamid MS, Hassen O (2019) Experimental and theoretical investigations of the lateral vibrations of an unbalanced Jeffcott rotor. *Front Struct Civ Eng* 14(5):1–9
43. Malgol A, Vineesh KP, Saha A (2022) Investigation of vibration characteristics of Jeffcott rotor system under influence of nonlinear restoring force, hydrodynamic effect and gyroscopic effect. *J Braz Soc Mech Sci Eng* 44(105):1–24
44. Genin J (1966) Effect of nonlinear material damping on whirling shafts. *Appl Sci Res* 15:1–11
45. Richardet GJ, Chatelet E, Baranger TN (2011) Rotating internal damping in the case of composite shafts. In: *IUTAM emerging trends in rotor dynamics*. IUTAM Book series. Springer. pp125–134 (978-94-007-0019-2)
46. Samantaray AK, Mukherjee A, Bhattacharyya R (2006) Some studies on rotors with polynomial type non-linear external and internal damping. *Int J Non-Linear Mech* 41(9):1007–1015
47. Shubin RCP, Malgol A, Saha A (2022) Effect of internal damping on the vibrations of a Jeffcott rotor system. In: *Banerjee S, Saha A (eds) Nonlinear dynamics and applications: springer proceedings in complexity*. Springer, Cham
48. Vatta F, Vigliani A (2008) Internal damping in rotating shafts. *Mech Mach Theory* 43(11):1376–1384
49. Afshari H, Torabib K, Jazi AJ (2022) Exact closed form solution for whirling analysis of Timoshenko rotors with multiple concentrated masses. *Mech Based Des Struct Mach* 50(3):969–992
50. Afshari H, Rahaghi MI (2018) Whirling analysis of multi-span multi-stepped rotating shafts. *J Braz Soc Mech Sci Eng* 40(9):1–17
51. Rahaghi MI, Mohebbi A, Afshari H (2016) Longitudinal-Torsional and two plane transverse vibrations of a composite Timoshenko rotor. *J Solid Mech* 8(2):418–434
52. Kandil MA (2004) On rotor internal damping instability. Ph.D. thesis, Department of Mechanical Engineering Imperial College, London, UK

Publisher's Note Springer Nature remains neutral with regard to jurisdictional claims in published maps and institutional affiliations.

Springer Nature or its licensor (e.g. a society or other partner) holds exclusive rights to this article under a publishing agreement with the author(s) or other rightsholder(s); author self-archiving of the accepted manuscript version of this article is solely governed by the terms of such publishing agreement and applicable law.